UNIVERSITY OF OKLAHOMA

GRADUATE COLLEGE

ASPECTS OF SEISMICITY CLUSTERING, SUBSURFACE STRUCTURE, AND STRESS ORIENTATIONS

A THESIS

SUBMITTED TO THE GRADUATE FACULTY

in partial fulfillment of the requirements for the

Degree of

MASTER OF SCIENCE

By

ANGIE ORTEGA ROMO
Norman, Oklahoma
2020

ASPECTS OF SEISMICITY CLUSTERING, SUBSURFACE STRUCTURE, AND STRESS ORIENTATIONS

A THESIS APPROVED FOR THE
SCHOOL OF GEOSCIENCES

BY THE COMMITTEE CONSISTING OF

Dr. Xiaowei Chen, Chair

Dr. Jacob Walter

Dr. Brett Carpenter

Acknowledgements

I would like to express my sincere gratitude to my committee members for their patience, guidance, motivation, and immense knowledge, especially to my research advisor Dr. Xiaowei Chen and committee member Jake Walter. I would also like to thank my research group, especially Yan Qin and Colin Pennington, for all their help in the completion of this project. Last but not least, I would like to thank my husband, mother, and other family members for their endless support and encouragement throughout the course of my Master's degree at the University of Oklahoma.

Table of Contents

Acknowledgements ..... **iv**

List of Tables ..... **vii**

List of Figures ..... **viii**

Abstract ..... **xi**

Chapter 1: Introduction ***1***

Chapter 2: Precursory Seismic Activities Leading up to Collapses During the 2018 Kilauea Volcanic Eruption ***3***

Introduction **3**

Data **4**

Methods **5**

Results **7**

Cluster analysis M1 7

Cluster analysis M2 7

Discussion **8**

Relationship between earthquakes and volcano activities 8

Relationship between earthquake rate and deformation rate 9

Conclusion **10**

Chapter 3: The Anatomy of the Cushing Fault Based on Earthquake Clustering and Crustal Reverberation ***19***

Introduction **19**

Data **20**

Methods **21**

Earthquake Cross-correlation 21

Relative Double Difference Relocation 21

Event Clustering 22

Crustal Reverberations Detection 22

Results **23**

HypoDD relocation 23

Similar event clusters 23

Characteristics of crustal reverberations 24

Discussion **25**

Conclusion **28**

Chapter 4: Spatially Distinct Tectonic Zones Across Oklahoma Inferred from Shear Wave Splitting ***42***

Introduction **42**

Data **43**

Method **43**
Results **45**
Spatial patterns of shear wave splitting from localized seismicity 47
Spatial patterns of shear wave splitting from regional seismicity 48
Temporal patterns of shear wave splitting 49
Discussion **51**
Conclusion **53**
Chapter 5: Conclusion ***67***
References **71**

List of Tables

Table 1. Iteration parameters for double difference relocation. * Last iteration to use the following weights †Weight P cross-correlation ‡ Weight S cross-correlation ¶ Weight P catalog § Weight S catalog ‖Residual threshold in seconds for cross-correlation data # Residual threshold in seconds for catalog data **Maximum distance in kilometers between cross-correlation linked pairs †† Maximum distance in kilometers between catalog linked pairs ‡‡Damping ...38
Table 2. Nine-layer 1D velocity model for Cushing fault zone adapted from Darold et al., (2015). * Depth of top of layer †Velocity.....39
Table 3. Crustal reverberations parameters in vertical channels. *Seismic station †Channel ‡Cluster number ¶Number of earthquakes per cluster §Number of peaks ||Amplitude ratio #Average depth in kilometers, rounded to the nearest hundredths **Average distance in kilometers, rounded to the nearest hundredths. 40
Table 4. Crustal reverberations parameters in horizontal channels. *Seismic station †Channel ‡Cluster number ¶Number of earthquakes per cluster §Number of peaks ||Amplitude ratio #Average depth in kilometers, rounded to the nearest hundredths **Average distance in kilometers, rounded to the nearest hundredths 41
Table 5. Shear wave splitting parameters database for Oklahoma and southern Kansas from localized seismicity at 35 seismic stations. †Primary fast direction of polarization. ‡Secondary fast direction of polarization. ¶Maximum shear stress orientations (Qin et al., 2019). *Maximum shear stress orientations (wsm). §Absolute difference between primary and secondary fast directions of polarization. ‖Absolute difference between primary fast direction of polarization and maximum shear stress orientations. All measurements are presented in degrees from north. 64
Table 6. Shear wave splitting parameters database for Oklahoma and southern Kansas from regional seismicity at 62 seismic stations. †Primary fast direction of polarization. ‡Secondary fast direction of polarization. ¶Maximum shear stress orientations (Qin et al., 2019). *Maximum shear stress orientations (wsm). §Absolute difference between primary and secondary fast directions of polarization. ‖Absolute difference between primary fast direction of polarization and maximum shear stress orientations. All measurements are presented in degrees from north. 66

List of Figures

Figure 1. Seismic activity at Kilauea volcano on Hawaii's main island. The seismic catalog (Shelly and Thelen, 2019) includes 44,188 high-resolution events (red dots) between April 29th and August 6th 2018. The yellow triangles denote the location of the tilt-meter stations and seismic station SDH and SMC. 12
Figure 2. Magnitude-frequency distribution, and b-value calculation for the seismic catalog (Shelly & Thelen, 2019). 13
Figure 3. Overview of clustering thresholds. (a) 2D density view of distance and time of nearest neighbors. The white solid lines show the thresholds used for the two clustering analyses with the main difference in distance. (b) Histogram of rescaled space distance with nearest neighbor events. (c) Histogram of time difference with nearest neighbor events. (d) Histogram of the combined space-time distance. The red vertical lines in (b), (c) and (d) mark the thresholds. 14
Figure 4. Overview of results from clustering analysis 1 with shorter space distance. For all figures, each cluster is marked with the same color. (a) and (b) are map view and depth view of clusters. The grey dots are non-clustered events, and the black circles denote events with M≥5. (c) magnitude versus time. (d) Number of events in each cluster versus time. (e) Normalized cumulative number of events versus time within each cluster. Clusters that have M≥5 events are shown as solid lines, and the other clusters are shown as dashed lines. (f) Duration versus time. 15
Figure 5. Overview of results from clustering analysis 2 with longer space distance. For all figures, each cluster is marked with the same color. (a) and (b) are map view and depth view of clusters. The grey dots are non-clustered events, and the black circles denote events with M≥5. (c) magnitude versus time. (d) Number of events in each cluster versus time. (e) Normalized cumulative number of events versus time within each cluster. Clusters that have M≥5 events are shown as solid lines, and the other clusters are shown as dashed lines. (f) Duration versus time. The black circles denote time separation between successive M≥5 earthquakes for comparison. 16
Figure 6. Summary of tiltmeter and earthquake rate relationship. (a) and (b): East (left axis) and North (right axis) tiltmeter data for stations SMC (a) and SDH (b). (c): earthquake rate and tilt rate for clusters with tiltmeter R-squared values ≥ 0.9 versus time. (d) and (e) are earthquake rate versus tilt rate for clusters before 2018/06/11 (d) and after 2018/06/21 (e). 17
Figure 7. Correlation between seismic waveform (orange), X-tiltmeter data (blue), Y-tiltmeter data (green), and earthquake magnitude (gray circles). Top: Correlation between seismic waveform, X-tilt data and Y-tilt data. Bottom: Correlation between seismic waveform amplitude and earthquake magnitude. (a) Cluster C1 (June 16th 04:21:00 to 20:41:00 hours), last approximately 16:20:00 hours and includes 127 earthquakes. (b) Cluster C2 (June 26th 06:46:00 hours to June 27th 08:41:00 hours), lasted approximately 25:55:00 hours and includes 391 events. 18
Figure 8. Map view of the study area. Cushing Fault Zone events (black dots) and stations that recorded crustal reverberations in one or more channel (triangles). The color of each station corresponds to the type of crustal reverberations (multiples) recorded: P multiples (red), S multiples (blue), P and S multiples (green). The outline color of each station corresponds to the type of recording station: seismic stations (black) or nanometric stations (white). 30

Figure 9. Comparison between the original Oklahoma Geological Survey (OGS) catalog (gray dots) and the double-difference relocated (HypoDD) catalog (black dots). Similar cluster events at station STN03, C1 – shallow cluster (blue circles), C2 – intermediate cluster (yellow circles), and C3 – deep cluster (red circles). (a) OGS catalog map view. (b) HypoDD catalog map view. (c) Map view comparison between OGS and HypoDD catalogs. (d) OGS catalog cross-section view. (e) HypoDD catalog cross-section view. (f) Cross-section view comparison between OGS and HypoDD catalogs. 31
Figure 10. Crustal reverberations on vertical channel (HHZ) at station STN03 for three clusters: C1- shallow depth cluster (blue), C2- intermediate depth cluster (yellow), and C3- deepest depth cluster (red). (a) Map view of C1, C2, and C3 in the Cushing Fault Zone. (b) Cross-section view of C1 (located around 1.60 km), C2 (located around 1.82 km), and C3 (located around 2.61 km). We suggest a dipping basement interface ranging from 1.6 km to 2.0 km. (c) Stacked waveforms for C1 (blue waveform), C2 (yellow waveform), and C3 (red waveform). (d) Stacked displacement waveforms for C1 (blue waveform), C2 (yellow waveform), and C3 (red waveform). 32
Figure 11. Crustal reverberations on horizontal channel (HH2) at station STN03 for three clusters: C1- shallow depth cluster (cyan), C2- intermediate depth cluster (purple), and C3- deepest depth cluster (magenta). (a) Map view of C1, C2, and C3 in the Cushing Fault Zone. (b) Cross-section view of C1 (located around 1.68 km), C2 (located around 1.91 km), and C3 (located around 2.80 km). We suggest a dipping basement interface ranging from 1.6 km to 2.0 km. (c) Stacked waveforms for C1 (cyan waveform), C2 (purple waveform), and C3 (magenta waveform). (d) Stacked displacement waveforms for C1 (cyan waveform), C2 (purple waveform), and C3 (magenta waveform). 33
Figure 12. Crustal reverberations on vertical channel (HHZ) at station STN33 for three clusters: C1- shallow depth cluster (blue), C2- intermediate depth cluster (yellow), and C3- deepest depth cluster (red). (a) Map view of C1, C2, and C3 in the Cushing Fault Zone. (b) Cross-section view of C1 (located around 1.64 km), C2 (located around 1.86 km), and C3 (located around 2.44 km). We suggest a dipping basement interface ranging from 1.6 km to 2.0 km. (c) Stacked waveforms for C1 (blue waveform), C2 (yellow waveform), and C3 (red waveform). (d) Stacked displacement waveforms for C1 (blue waveform), C2 (yellow waveform), and C3 (red waveform). 34
Figure 13. Crustal reverberations on horizontal channel (HH1) at station STN33 for two clusters: C1- shallow depth cluster (cyan) and C2 - deep depth cluster (purple). (a) Map view of C1and C2 in the Cushing Fault Zone. (b) Cross-section view of C1 (located around 1.66 km) and C2 (located around 2.41 km). We suggest a dipping basement interface ranging from 1.6 km to 2.0 km. (c) Stacked waveforms for C1 (cyan waveform) and C2 (purple waveform). (d) Stacked displacement waveforms for C1 (cyan waveform) and C2 (purple waveform). 35
Figure 14. (a) Map view of stations in central Oklahoma that recorded crustal reverberations on one or more channels from the Cushing sequence (black dots). Stations that recorded P wave crustal reverberations (white outline), S wave crustal reverberations (blue outline), and P and S wave crustal reverberations (black outline). The color of each station corresponds to the color of waveform in panels (b) and (c). (b) Stacked waveforms for nine stations that recorded P wave crustal reverberations sorted by distance. (c) Stacked waveforms for five stations that recorded S wave crustal reverberations sorted by distance. 36
Figure 15. Oklahoma Geological Survey (OGS) catalog (red dots) and double-difference relocated (HypoDD) catalog (black dots) comparison for Cushing sequence and M4.4 event

(blue circle) and M5.0 (magenta circle). (a) OGS catalog map view. (b) HypoDD catalog map view. (c) OGS catalog cross-section view. (d) HypoDD catalog cross-section view.....37
Figure 16. Oklahoma map displaying the seismic sequence distribution (blue dots) between 2010 and 2019, the fault systems (gray lines), and the stations location included in this study (red triangles). The interest areas are as follows: 1. Kansas: stations KAN01 and KAN10 (orange); 2. Fairview: stations FW03 and OK039 (green); 3. Pawnee: stations PW11 and PW14 (yellow); 4. Central Oklahoma: stations FNO and SMO (cyan). 54
Figure 17. Localized seismicity results. Regional map of Oklahoma and southern Kansas seismic network showing primary (black) and secondary (white) ϕ directions at each station. Polar histograms for the six isolated stations. Kansas (orange): KAN01 (ϕ_{pri}:18° – ϕ_{sec}: 48°) and KAN10 (ϕ_{pri}:66° – ϕ_{sec}: -54°). Fairview (green): FW03 (ϕ_{pri}: -54° – ϕ_{sec}: 60°) and OK039 (ϕ_{pri}: -73° – ϕ_{sec}: 36°). Pawnee (yellow): PW11 (ϕ_{pri}: 6° – ϕ_{sec}: 78°) and PW14 (ϕ_{pri}: 78° – ϕ_{sec}: 18°). Central Oklahoma (cyan): FNO (ϕ_{pri}: 95° – ϕ_{sec}: 5°) and SMO (ϕ_{pri}: 61° – ϕ_{sec}: -46°)...55
Figure 18. Regional seismicity results. Regional map of Oklahoma and southern Kansas seismic network showing primary (black) and secondary (white) ϕ directions at each station. Polar histograms for the six isolated stations. Kansas (orange): KAN01 (ϕ_{pri}: -12° – ϕ_{sec}: 78°) and KAN10 (ϕ_{pri}: -18° – ϕ_{sec}: 72°). Fairview (green): FW03 (ϕ_{pri}: -51° – ϕ_{sec}: 53°) and OK039 (ϕ_{pri}: -72° – ϕ_{sec}: 36°). Pawnee (yellow): PW11 (ϕ_{pri}: 78° – ϕ_{sec}: -6°) and PW14 (ϕ_{pri}: 78° – ϕ_{sec}: 18°). Central Oklahoma (cyan): FNO (ϕ_{pri}: 90° – ϕ_{sec}: 0°) and SMO (ϕ_{pri}: 60° – ϕ_{sec}: -42°)...56
Figure 19. Fast polarization directions over time. 2D histograms for four of the isolated stations: KAN01, RH11, OK035, FNO, X37A, and WMOK. On the vertical axis, the data is divided into 30 bins, where each bin is 6 degrees long. On the horizontal axis, the data is divided into 20 number of bins, where each bin is 0.5 years long. 57
Figure 20. Regional comparison between primary (black) and secondary (white) ϕ directions from localized seismicity and σmax orientations. Red dashed line: world stress map (wsm) measurements. Red solid line: Qin et al., (2019) measurements. 58
Figure 21. Regional comparison between primary (black) and secondary (white) ϕ directions from regional seismicity and σmax orientations. Red dashed line: world stress map (wsm) measurements. Red solid line: Qin et al., (2019) measurements. 59
Figure 22. Statistical analysis of fast polarization directions (ϕ) in southern Kansas and comparison with average regional σmax orientations (Qin et al., 2019). (a) Localized seismicity. (b) Regional seismicity. 60
Figure 23. Statistical analysis of fast polarization directions (ϕ) in Pawnee and comparison with average regional σmax orientations (Qin et al., 2019). (a) Localized seismicity. (b) Regional seismicity. 61
Figure 24. Statistical analysis of fast polarization directions (ϕ) in Fairview and comparison with average regional σmax orientations (Qin et al., 2019). (a) Localized seismicity. (b) Regional seismicity. 62
Figure 25. Statistical analysis of fast polarization directions (ϕ) in central Oklahoma and comparison with average regional σmax orientations (Qin et al., 2019). (a) Localized seismicity. (b) Regional seismicity. 63

Abstract

I study aspects of seismicity clustering, subsurface structures and stress orientations by analyzing seismicity at two of the most seismically active regions in the USA (Hawaii and Central USA). The notable volcanic, seismic, and collapsing activities at the summit of Kilauea volcano in 2018, provided a significant opportunity to observe and quantify naturally occurring earthquake clusters and their characteristics. I perform a spatiotemporal clustering analysis of the high-resolution earthquake catalog presented by *Shelly and Thelen (2019)* following the nearest neighbor workflow in *Cheng and Chen (2018)*. We identify two modes (M1 and M2) of naturally occurring earthquake clusters. M1 focuses on restricted time and distance separation with: $\eta = 0.0316, R = 0.0562\ km, T = 0.1\ day$. It consists of 45 clusters (20+ events). M1 clusters do not show clear temporal correlation with collapsing events (M≥5) and are found as isolated patches of seismicity off the main crater. M2 focuses on time separation with $\eta = 0.0316, R = 6.3096\ km, T = 0.1\ day$ finding 42 clusters (20+ events). M2 clusters can be defined as a seismicity cycles, where the collapsing events (M5.2 – M5.4) mark the end of the cycle. M2 clusters identify the precursory activities leading up to major collapsing events and corresponds to the deformation activity (tilt rate) at the summit of Kilauea volcano. On the other hand, the central USA has experienced significant seismicity rate fluctuations over the last decade (*Schoenball & Ellsworth, 2017*). A key question to better understand the triggering mechanism is the relative depth to basement and injection layer. However, determining absolute depth is challenging due to station coverage and imperfect 1D velocity models. In this study, I analyze crustal reverberations (reflection within the upper sedimentary layer) to improve earthquake depths estimation for the Cushing fault zone sequence. I use waveform cross-correlation to group events into different similar event clusters, then I obtain double difference relative locations and examine waveform

signatures of different clusters. Upon careful examination, I find that events originated at different depth have different amplitudes of reverberations. For Cushing sequence, I identify a narrow layer at shallow depth, likely representative of more weathered portion of the top of crystalline basement. To execute a regional spatial analysis of fast polarization directions (ϕ) in the central U.S.A. I use the shear wave splitting (SWS) technique to measure SWS parameters (fast direction [ϕ] and delay time [dt]). I use 33,367 local earthquakes recorded from 2010 to 2019 and the automated SWS software MFAST (*Savage et al., 2010*) to calculate SWS parameters. I successfully calculate 524,395 splits. The high-quality measurements provide a complete localized and regional dataset of SWS measurements for the Central U.S.A. All stations in this study present two directions of fast polarization, primary (ϕ_{pri}) and secondary (ϕ_{sec}). The presence of these ϕ_{sec} is potentially caused by local stress perturbations and shear-fabric alignments. At the regional level, either ϕ_{pri} or ϕ_{sec} correlate with the maximum stress orientation (σ_{max}) in the region. However, many sub-regions show a clear deviation between ϕ and σ_{max} directions. These discrepancies are potentially caused by local structures.

Chapter 1: Introduction

This research project focuses on two very seismically active regions in the USA: Hawaii and central USA. I conducted three independent research studies to better understand earthquake clustering, subsurface structures and stress orientations. In the first study, I analyzed naturally occurring clusters at Kilauea volcano in Hawaii's main island. In the second study, I observed and analyzed earthquake crustal reverberations at the Cushing fault zone in Oklahoma, and on the third and last study I performed a regional shear wave splitting analysis in Oklahoma and southern Kansas.

In Hawaii, I studied the seismic, collapsing, and volcanic activities associated with one of the most active volcanoes in the world, Kilauea volcano (*USGS, 2019*). On May 4th, 2018 a major seismic event of Mw6.9, occurred in the fault zone near Hawaii's main island, which is the largest event in Hawaii in the last 43 years (*Neal et al., 2019*). Since May 3rd 2018 a series of seismic events, caldera collapses, and explosions occurred progressively and lasted until August 2018 (*Shelly & Thelen, 2019*). For this first part of the study, I focus on precursory seismic activity leading to major caldera collapses at the summit of Kilauea volcano. A clustering analysis technique (*Cheng and Chen, 2018*), based on the nearest neighbor method in both time and space domains, was performed to link seismic events as clusters. The results of this study show that the increase in seismic activity, clustering and collapsing behavior correlates well with the volcanic activity at Kilauea volcano during this period.

On the other hand, the central USA, specially the state of Oklahoma, has experienced a significant increase in seismicity over the last decade, mostly due to anthropological activities like wastewater disposal and hydraulic fracturing (*Keranen et al., 2014; Schoenball & Ellsworth, 2017*). In the second study, I analyzed crustal reverberations on individual channels to better

constrain focal depths for earthquakes at the Cushing fault zone in Oklahoma. I applied the waveform cross-correlation technique to group events into clusters based on waveform similarity on vertical and horizontal channels at each seismic station in the area. In the stacked trace of each cluster, I detected crustal reverberations by cross-correlating the direct P–wave or S-wave arrival along the stacked trace with a moving time window. Once these crustal reverberations were detected, I calculated the delay time and amplitude ratio between each reverberation and the direct wave arrival. I also use an earthquake relocation program HypoDD (*Waldhauser and Ellsworth, 2000*) to improve the relative locations of the events and to provide a better preliminary earthquake source depth for this earthquake sequence. The obtained results show that events originated at different depths have different amplitude ratios but relative constant delay time.

In the third and last study, I apply the shear wave splitting technique to identify spatial patterns or crustal anisotropy and stress orientation in Oklahoma and southern Kansas. To calculate the shear wave splitting parameters, I used the automated shear wave splitting software MFAST (*Savage et al., 2010*). This study focuses on the spatial analysis of the fast direction of polarization (ϕ) in Oklahoma and southern Kansas. The results of this study show that most stations have a primary fast direction of polarization (ϕ_{pri}) and secondary fast direction of polarization (ϕ_{sec}). At most stations either the primary fast direction of polarization (ϕ_{pri}) or the secondary fast direction of polarization (ϕ_{sec}) is consistent with the shear stress (σ_{max}) orientations around the USA mid-continent. However, there are some discrepancies between fast polarization directions (ϕ) and shear stress orientations (σ_{max}) probably caused by local stress perturbations in the region. No significant stress direction changes over time were detected with this technique.

Chapter 2: Precursory Seismic Activities Leading up to Collapses During the 2018 Kilauea Volcanic Eruption

Introduction

The Kilauea volcano located on Hawaii's main island has erupted 34 times since 1952, making it one of the most active volcanoes in the world (*USGS, 2019*). According to USGS, eruptive activity along Kilauea volcano's East Rift Zone (ERZ) was nearly continuous from 1983 to 2018. On April 30th 2018, a dike intrusion in the ERZ ended the 35-yearlong continuous eruption of Kilauea volcano (*Anderson et al., 2019*). On May 3rd 2018, the dike intrusion and a major volcanic eruption triggered a major outpouring of lava in the ERZ, which is located approximately 40 kilometers away from the volcano's summit. More than 1 km^3 of lava was erupted, destroying hundreds of properties and putting thousands of civilians at risk (*Anderson et al., 2019*). Since then, a series of caldera collapses, explosions, and seismic events occurred progressively and lasted for three months until August 2018 (*Shelly & Thelen, 2019*). On May 4th, 2018 a major seismic event of Mw6.9, occurred in the fault zone near Hawaii's main island, which is the largest event in Hawaii in the last 43 years (*Neal et al., 2019*).

The Kilauea summit's collapsing sequence is the best documented sequence in the world with the largest comprehensive dataset (*Shelly & Thelen, 2019*). This dataset includes a multi-parameter monitoring network, including ground deformation measurements with borehole tilt-meters, InSAR, GPS, LiDAR and GNSS (*Neal et al., 2019; Shelly & Thelen, 2019*). A total of 62 collapses were recorded between May and August 2018, these collapses are estimated in 825 million m^3 at Kilauea volcano, which is the largest amount in the last 200 years (*Anderson et al., 2019; Neal et al., 2019*). The deformation associated with the collapsing sequence suggests a considerable amount of magma drainage from the shallower reservoir towards the rift zone (*Neal et al., 2019*). During this sequence, each caldera collapse terminates a seismic cycle that includes

hundreds of magnitude Mw3.0 – Mw 4.0 summit events, or thousands of events if we consider micro seismic events (*Shiro et al., 2018*). The caldera collapses are generally associated with a Mw 5.2 – Mw 5.4 seismic events that occurred almost on a daily basis (*Butler, 2019; Neal et al., 2019; Segall et al., 2019; Shelly & Thelen, 2019*), making it an ideal sequence to perform clustering analysis.

Seismic clustering analysis provides key information on earthquake dynamics based on the spatiotemporal behavior of the seismic events (*Zaliapin & Ben-Zion, 2013*). In this study, we perform a spatiotemporal clustering analysis using the high-resolution earthquake catalog presented by *Shelly and Thelen (2019)*. We focus on the precursory seismic activity leading to the summit collapses at Kilauea volcano during the period of highest seismicity rate from May to August 2018. The clustering analysis follows the nearest neighbor workflow in *Cheng and Chen (2018)*. With this clustering technique we aim to quantify and characterize naturally occurring clusters and their direct relationship with the volcanic activity at Kilauea volcano. After executing the clustering analysis, we examine the temporal variation of cluster characteristics and their relationship with tilt-meter data from two nearest tilt-meter stations and volcanic activities observed at the summit of Kilauea volcano.

Data

We use the earthquake catalog from *Shelly and Thelen (2019)*. The matched-filter detected and relocated catalog consists of 44,188 events associated to seismic activity at the summit of Kilauea volcano between April 29th and August 6th 2018 (Figure 1). Most of the events are located from 0 to 2.5 kilometers deep. The event magnitudes range from Mw -1.17 to Mw 5.4, including both micro-seismic events and major events associated with caldera collapses. For analysis in this

study, only events above the magnitude of completeness (Mc = 1.8) are considered (Figure 2). The magnitude frequency distribution of the catalog exhibits two trends: (1) events below Mw4.3 can be well explained with Gutenberg-Richter relationship with a b-value of about 0.94 (*Gutenberg & Richter, 1942*); (2) excess of larger events with Mw≥4.3 (Figure 2) that are potentially associated with major collapse events (*Shelly & Thelen, 2019*).

Tilt-meter datasets from borehole stations SDH (south of the summit) and SMC (east of the summit) were obtained from the Hawaii Volcano Observatory (HVO) (Figure 1). The tilt-meter data provides slope inclination measurements over time in both east (X) and north (Y) directions from April 30th to August 5th 2018.

Methods

Earthquake clustering provides information about interactions among seismic events. To fully understand the seismicity behavior at the summit of the Kilauea Volcano during the eruption, we perform clustering analysis following *Cheng and Chen (2018)*. This method is based on nearest-neighbor distance approach, using a single-link method to cluster events with the smallest spatial and temporal separation.

First, we obtain the combined spatiotemporal distance between all event pairs (event *i* and *j*) following *Zaliapin and Ben-Zion (2013)* and *Cheng and Chen (2018)*:

$$\eta_{ij} = dt_{ij} \times dr_{ij}^{d}, \; dt_{ij} > 0;$$

$$\eta_{ij} = \infty, \qquad dt_{ij} \leq 0,$$

where, d is the fractal dimension of the epicenters, a value of 1.6 from *Cheng and Chen (2018)* is chosen, dt_{ij} represents the interevent time in days and dr_{ij} the interevent epicentral distance (*Cheng & Chen, 2018*).

Then, we search for the nearest neighbor for each event *j* that have the smallest η that occurred before *j*.

Finally, we represent the spatial and temporal component between event *j* and its nearest neighbor event *k* by

$$T_{kj} = dt_{kj}\ ;\ R_{kj} = dr_{kj}^{d}$$

In Figure 3a, we clearly see a bimodal distribution of nearest neighbor distances from the 2D density plot: mode 1 with longer inter-event time but shorter inter-event distance and mode 2 with relatively shorter inter-event time but longer inter-event distance. When examining the histograms of neighboring distances, both the combined distance η and time difference T appear as single-mode (Figure 3c and 3d), but the distance difference R shows clear bimodal distribution (Figure 3b).

Based on the observations, we perform two clustering analyses:

(1) M1: focus on mode 1, and consider both time and restricted distance separation with: $\eta = 0.0316, R = 0.0562\ km, T = 0.1\ day$. The shorter spatial distance separation would potentially allow us to identify individual faults with highly concentrated seismicity.

(2) M2: focus on the time separation with $\eta = 0.0316, R = 6.3096\ km, T = 0.1\ day$. Previous studies suggest that the microseismicity exhibit cyclic behavior with strong clustering in time (*Shelly & Thelen, 2019*), this allows us to identify both mode 1 and mode 2. The rescaled distance of 6.3096 km corresponds to 3.94 km in absolute distance.

For each parameter set, we define clusters based on the single-link method used in *Cheng and Chen, (2018)*. For clusters with more than 20 events, we obtain the total number of events and cluster duration (defined as the duration contains 95% of the events). In addition, for each cluster, we obtain the corresponding tilt-meter data from the East and North directions from stations SDH

and SMC. Visual inspection suggests that both event number and tilt changes follow constant rate increase during each cluster, therefore, we perform linear fitting for both event growth and tilt amount change with time for each cluster. The result of linear fitting is used to discuss the relationship between earthquake rate and deformation rate during each cluster.

Results

Cluster analysis M1

This analysis focuses on shorter spatial distance, and found 1,157 clusters. Histogram of number of events within each cluster shows a power law decay relationship, with about 500 clusters with 2 events, and about 10 clusters with 10 events. Figure summarizes distributions of 45 clusters with more than 20 events. Figure 4a and 4b shows the map view and depth view of identified clusters. With the shorter distance criterion, the clusters are concentrated within several isolated patches off the main crater center. There is no clear temporal correlation between individual cluster and occurrence of M≥5 collapse events. These clusters tend to peak during two time periods: around June 20th to June 26th, and July 24th to July 26th. The first-time period corresponding to a transition between ash producing collapses and non-ash producing collapses (the alert level was changed from red to orange on June 24) (*USGS, 2018*). The second-time period corresponds to the end of the collapsing sequence. It is possible that these events occur within boundary faults and almost all events occur within 160m of another event with these fault patches.

Cluster analysis M2

This analysis focuses on the time separation, where all events within the caldera that are within 0.1 day of their nearest neighbor can fall within the same cluster. This results with 166 clusters, and 55 clusters with more than 20 events. In comparison to M1 results (Figure 4), where

only isolated patches are identified, Figure 5 shows that most of these events fall within clusters with more than 20 events. Out of the 44 events with M≥5, 42 events fall within one of the 55 clusters, and are always the last event of these clusters (the two events that do not fall within clusters occurred on May 30th and June 4th). This indicates that the temporal clustering analysis identifies the precursory activities leading up to major collapsing events. Figure 5f shows that the duration of these clusters corresponds well with time separation between successive M≥5 earthquakes.

Figure 5e shows (mostly) linear increase of event numbers with time. Linear regression analysis finds that the event growth with time for all the clusters can be well explained with constant event rate (R-square values are all greater than 0.9 using "*fitlm*" function in MATLAB). The cluster duration gradually increases with time, from the about 0.5 days at the beginning to 1.5 days towards the end of the eruption sequence (Figure 5f), which can also be visualized in Figure 5e through the gradual color changes. Event number per cluster rapidly increased around June 11th (Figure 5d), which is the time when the highly compacted spatial clusters started to occur (Figure 4d). Event number per cluster peaked around June 21st (Figure 5d), consistent with the peak time of clustering with shorter distances (Figure 4d).

Discussion

Relationship between earthquakes and volcano activities

From Figure 4d and 5d, it appears that there are two important dates related to changes in event clustering characteristics: June 11th and June 21st. The first date corresponds to rapid increase in precursory seismicity and appearance of isolated fault patches with large number of earthquakes. This likely suggests activation of major boundary faults surrounding the caldera. Based on

chronology of volcano activities, on June 10th and 11th, major changes in eruption at fissure 8 occurred with three closely spaced lava fountains erupting at large heights (*USGS, 2018*). The second-time stamp corresponds to a period when collapse events transition from ash-producing to non-ash producing, suggesting a possible transition in how the caldera system accommodates deformations (*USGS, 2018*).

The gradual increase in cluster duration correlates well with the gradual increase in the intervals between M≥5 events (collapses events). However, the cluster duration is systematically shorter than M5 event interval by about 0.5 days, which suggests a period of quiescence after major collapsing events (Figure 5f), consistent with visual observations in *Shelly and Thelen, (2019)*. The increased cluster duration suggests that the caldera system requires longer time for re-pressurization following each collapse events as the magma chamber is depleting.

Relationship between earthquake rate and deformation rate

Linear regression analysis is performed for tilt-meter data during each cluster period. The tilt-meter is sampled at 60 seconds. Because of the short-term fluctuations (Figure 6), data is smoothed for every 3 hours before linear fitting. Time periods with R-squared greater than 0.9 can be considered as having constant deformation rates. East and North components from two nearest tilt-meter stations (SDH and SMC) are analyzed (Figure 6). The linear regression analysis suggests that the east component of station SDH has the most time periods that meet linear approximation criteria (R-square ≥ 0.9), which is then used for analysis between earthquake rate and deformation rate. A complete geodetic analysis is beyond the scope of this paper. The purpose of the analysis here is to understand the controlling factors of earthquake rates during each cycle.

Figure 6 shows that station SDH started to have large amplitude short-term fluctuations two days before June 11th, corresponding to the activation of isolated fault patches. Detailed

inspection of two example clusters (Figure 7) shows that these large fluctuations are likely associated with relatively larger earthquakes (e.g., M≥3). Figure 6d shows that before June 11th, there is a negative correlation between earthquake rate and tilt rate. The negative correlation and absence of active fault patches suggests that most of the deformation during this period are aseismic, likely due to volcano inflation/deflation.

On June 21st, both cluster event number and tilt rate at station SMC experienced peak values. Following June 21st, earthquake rate during each cluster decreases with decreased tilt rate, and tilt rate gradually flattens towards the end of the sequence (Figure 6c). The lowered alert level of the volcano (due to absence of ash producing collapses) and positive correlation between earthquake rate and deformation rate (Figure 6e) suggests that much of the deformation is accommodated by boundary faults activated during the eruption.

Conclusion

The significant seismic, volcanic, and collapsing activities at the summit of Kilauea volcano in 2018, provide an incredible opportunity to observe and quantify two modes (M1 and M2) of naturally occurring clusters and their empirical characteristics. For M1 (shorter space distance), 1,157 clusters are identified of which 45 clusters have 20 or more events. These clusters are characterized for being found in isolated patches off the main crater and not having a clear temporal correlation between individual clusters and collapses events (M≥5). M1 clusters show a direct correlation between the summit collapsing activity behavior (e.g. ash producing collapses, non-ash producing collapses, end of the collapsing sequence, etc.) to the peak clustering formation. On the contrary, M2 (longer space distance) clustering results focus on the time separation of the events. For this mode, 166 clusters were identified, where 55 clusters have 20 or more events and

42 clusters out of the 55 can be defined as a seismicity cycle. The beginning of the cycle is characterized by a period of latent seismicity, followed by a period of significant seismicity increase and finalizing with a Mw5.2 – Mw5.4 caldera collapse. Indicating that this temporal clustering analysis identifies the precursory activities leading up to major collapsing events. The cluster duration gradually increases with time, from about 0.5 days at the beginning to 1.5 days towards the end of the eruption sequence. M2 clustering behavior is directly correlated to the volcanic activity at Kilauea volcano, specifically to the summit deformation due to pressure decrease in the magma reservoir measured by borehole tilt-meter stations. Along the sequence, correlation between earthquake rate and deformation rate suggests that much of the deformation is accommodated by boundary faults activated during the eruption. In the contrary, negative correspondence between tilt rate and earthquake rate suggest that most of the deformation during this period is aseismic, likely due to volcano inflation/deflation.

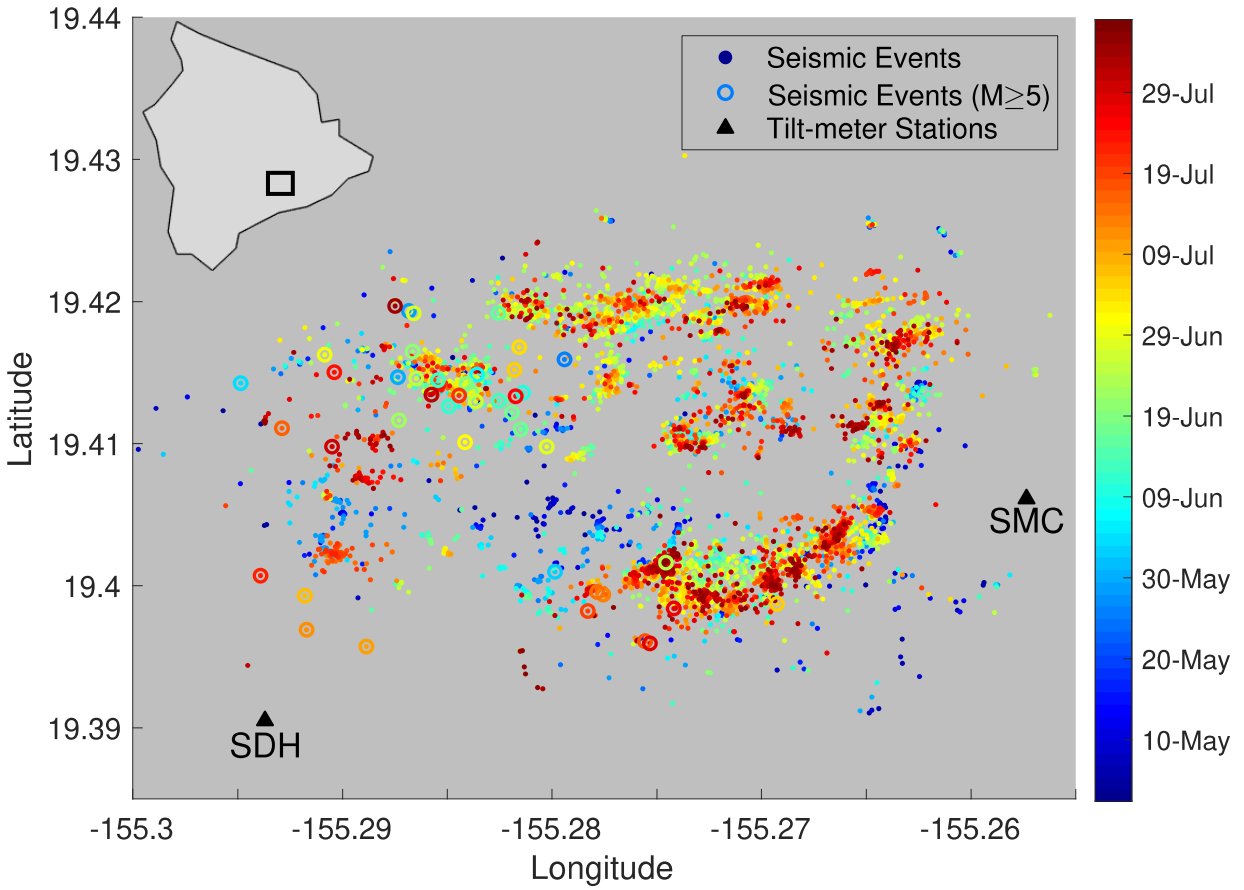

Figure 1. Seismic activity at Kilauea volcano on Hawaii's main island. The seismic catalog *(Shelly and Thelen, 2019)* includes 44,188 high-resolution events (red dots) between April 29th and August 6th 2018. The yellow triangles denote the location of the tilt-meter stations and seismic station SDH and SMC.

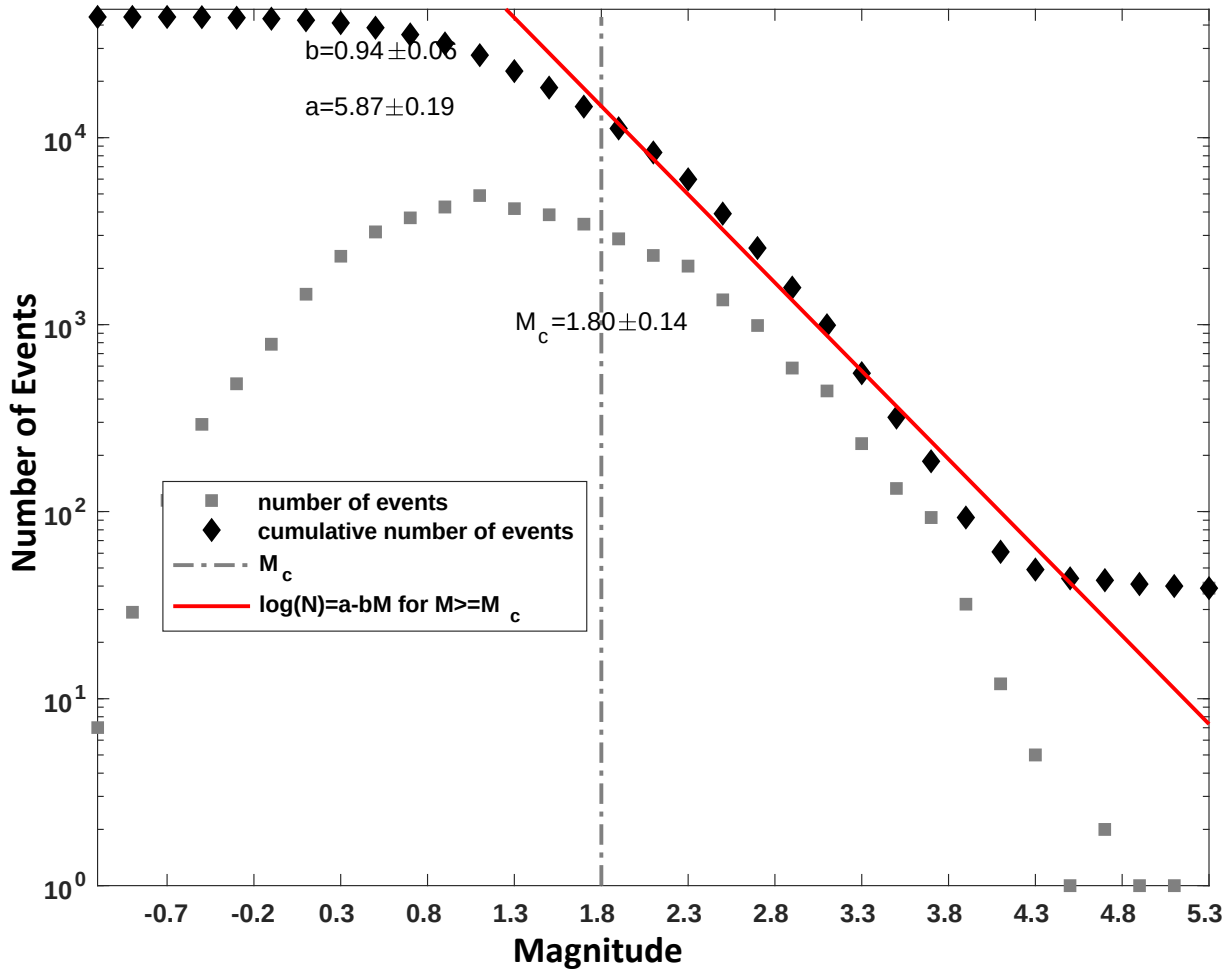

Figure 2. Magnitude-frequency distribution, and b-value calculation for the seismic catalog (*Shelly & Thelen, 2019*).

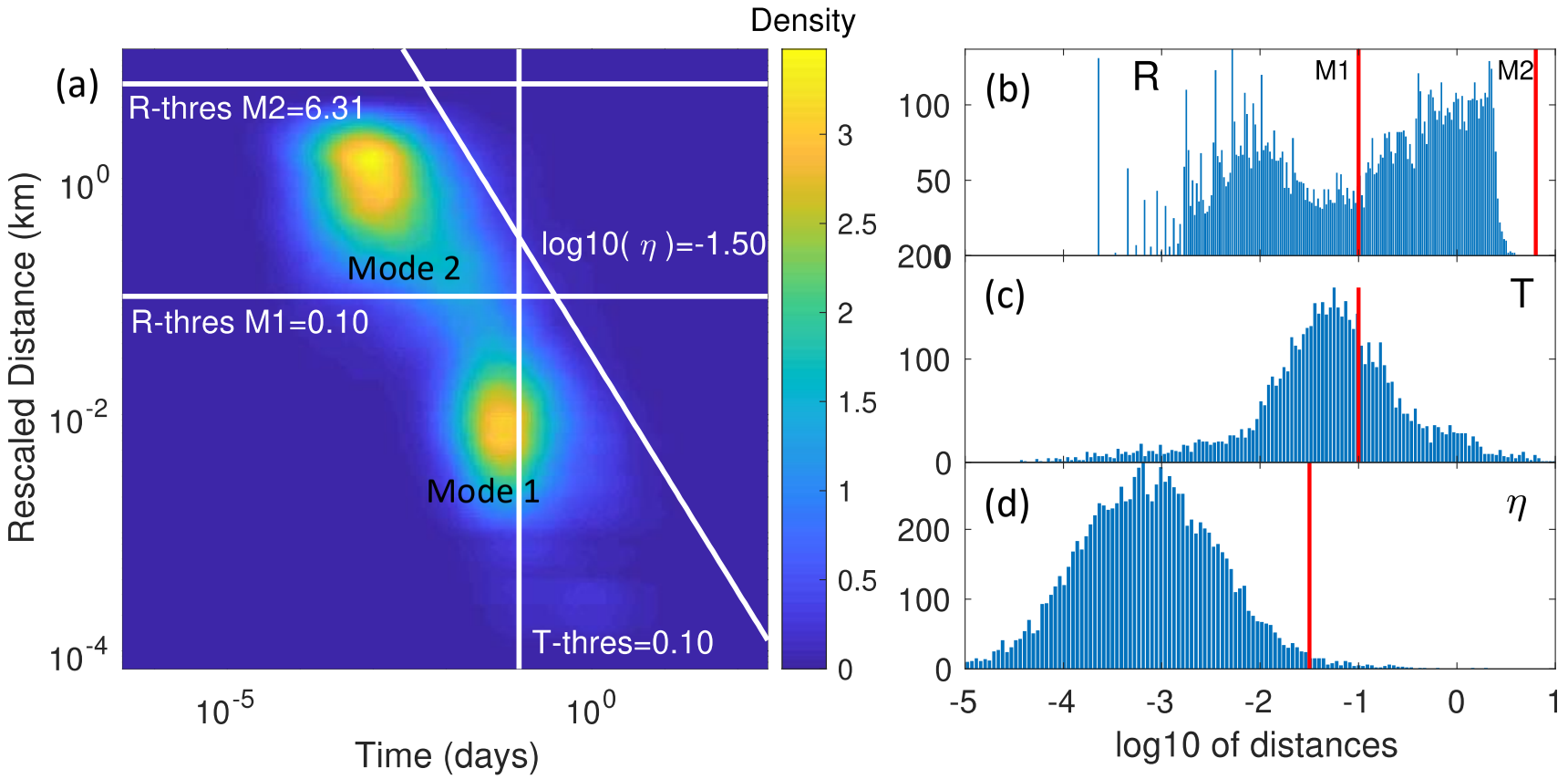

Figure 3. Overview of clustering thresholds. (a) 2D density view of distance and time of nearest neighbors. The white solid lines show the thresholds used for the two clustering analyses with the main difference in distance. (b) Histogram of rescaled space distance with nearest neighbor events. (c) Histogram of time difference with nearest neighbor events. (d) Histogram of the combined space-time distance. The red vertical lines in (b), (c) and (d) mark the thresholds.

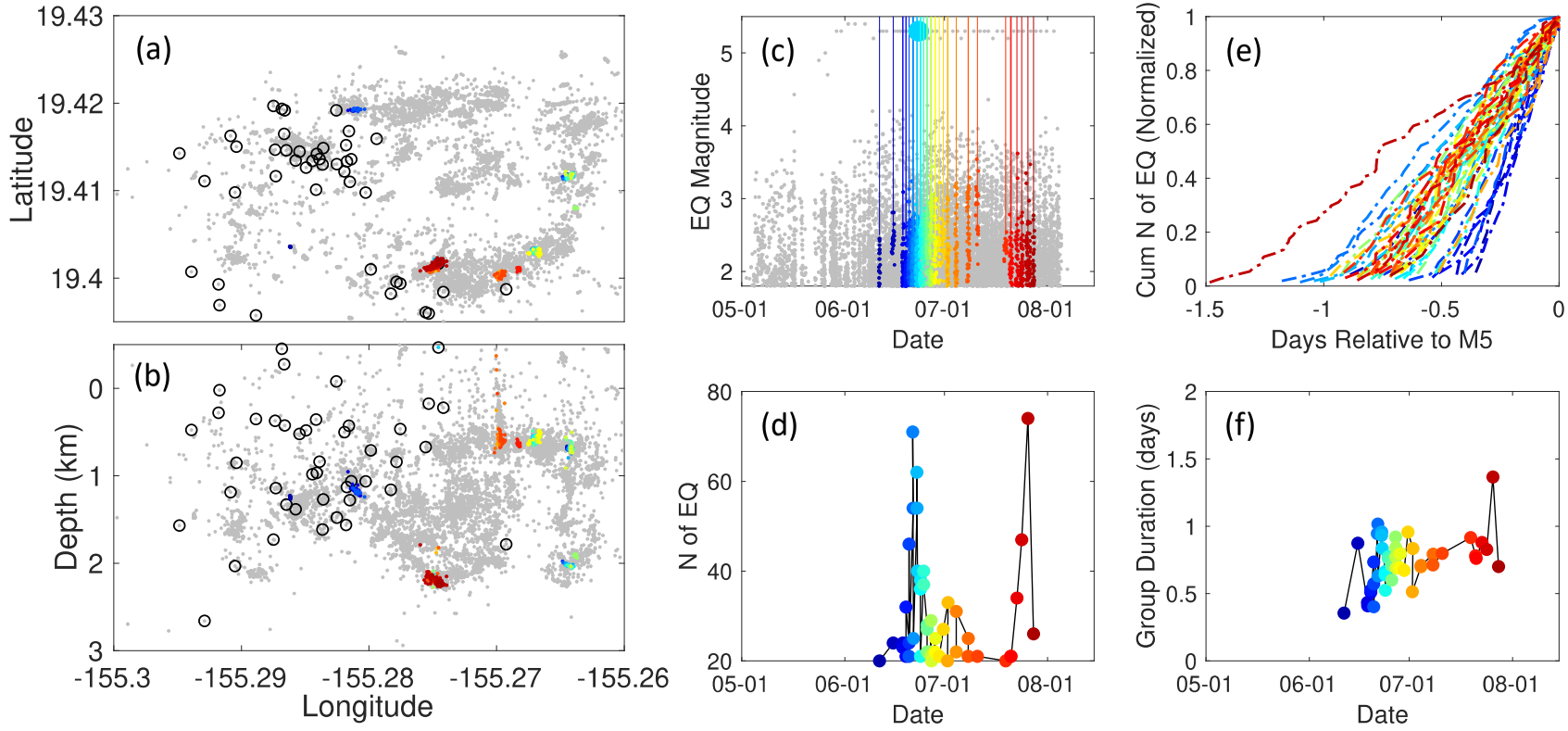

Figure 4. Overview of results from clustering analysis 1 with shorter space distance. For all figures, each cluster is marked with the same color. (a) and (b) are map view and depth view of clusters. The grey dots are non-clustered events, and the black circles denote events with M≥5. (c) magnitude versus time. (d) Number of events in each cluster versus time. (e) Normalized cumulative number of events versus time within each cluster. Clusters that have M≥5 events are shown as solid lines, and the other clusters are shown as dashed lines. (f) Duration versus time.

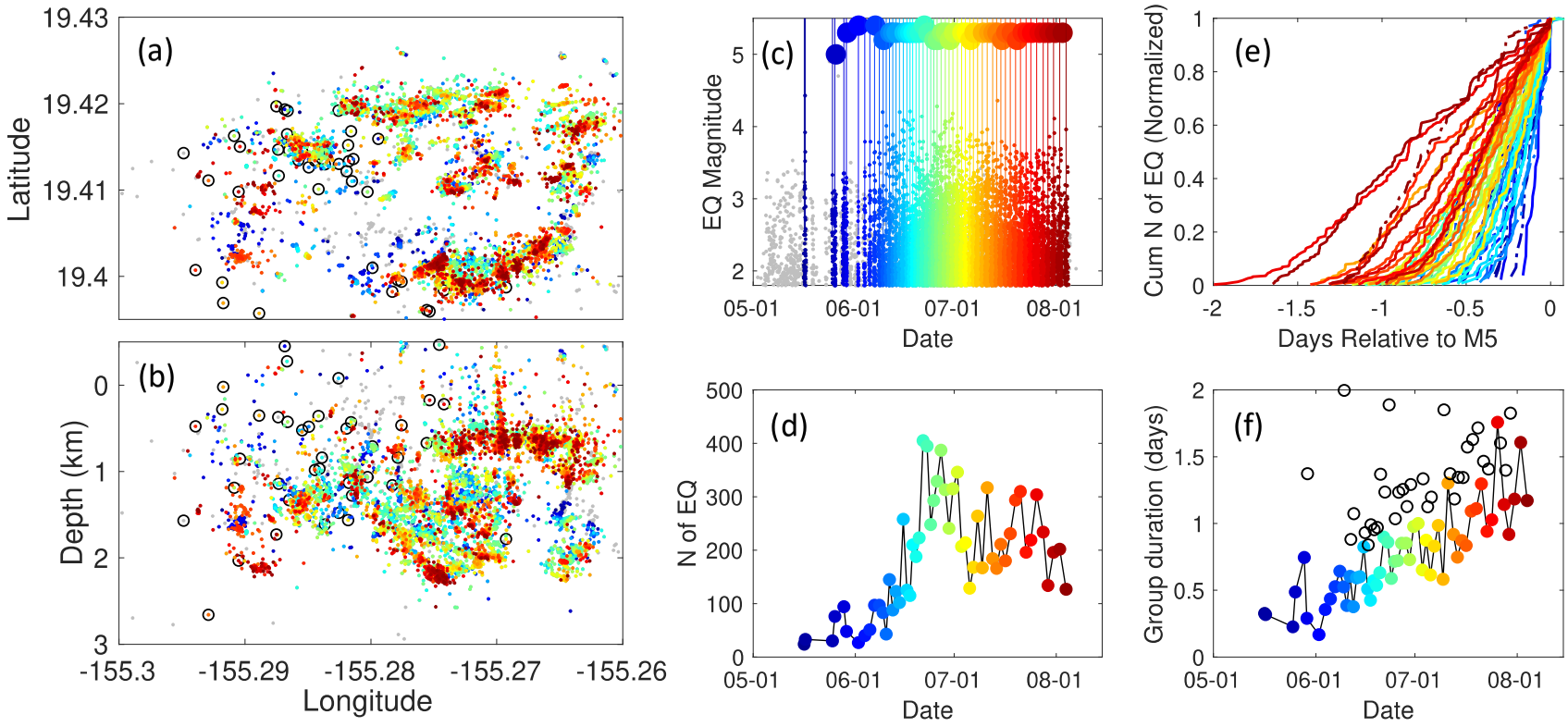

Figure 5. Overview of results from clustering analysis 2 with longer space distance. For all figures, each cluster is marked with the same color. (a) and (b) are map view and depth view of clusters. The grey dots are non-clustered events, and the black circles denote events with M≥5. (c) magnitude versus time. (d) Number of events in each cluster versus time. (e) Normalized cumulative number of events versus time within each cluster. Clusters that have M≥5 events are shown as solid lines, and the other clusters are shown as dashed lines. (f) Duration versus time. The black circles denote time separation between successive M≥5 earthquakes for comparison.

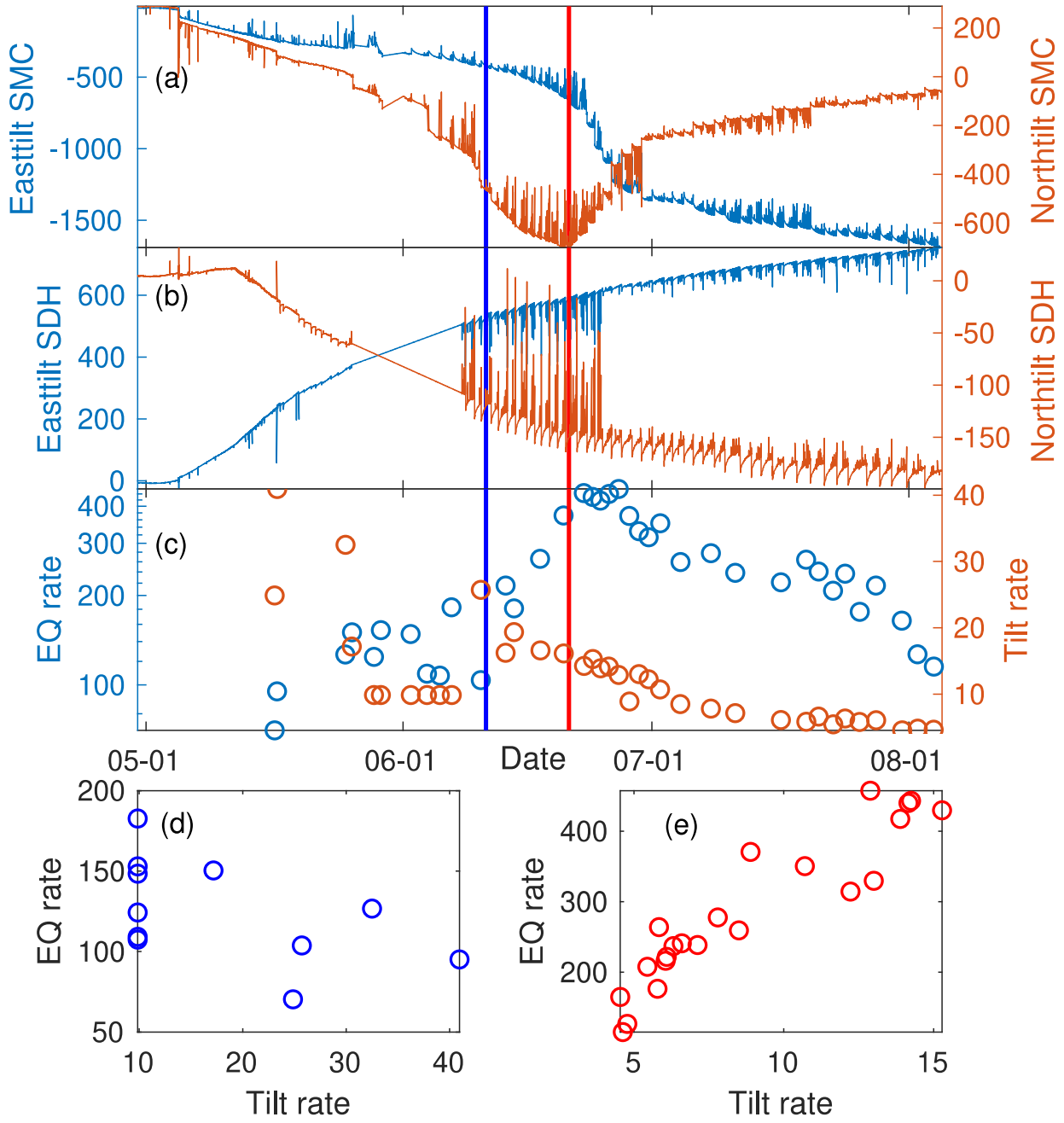

Figure 6. Summary of tiltmeter and earthquake rate relationship. (a) and (b): East (left axis) and North (right axis) tiltmeter data for stations SMC (a) and SDH (b). (c): earthquake rate and tilt rate for clusters with tiltmeter R-squared values ≥ 0.9 versus time. (d) and (e) are earthquake rate versus tilt rate for clusters before 2018/06/11 (d) and after 2018/06/21 (e).

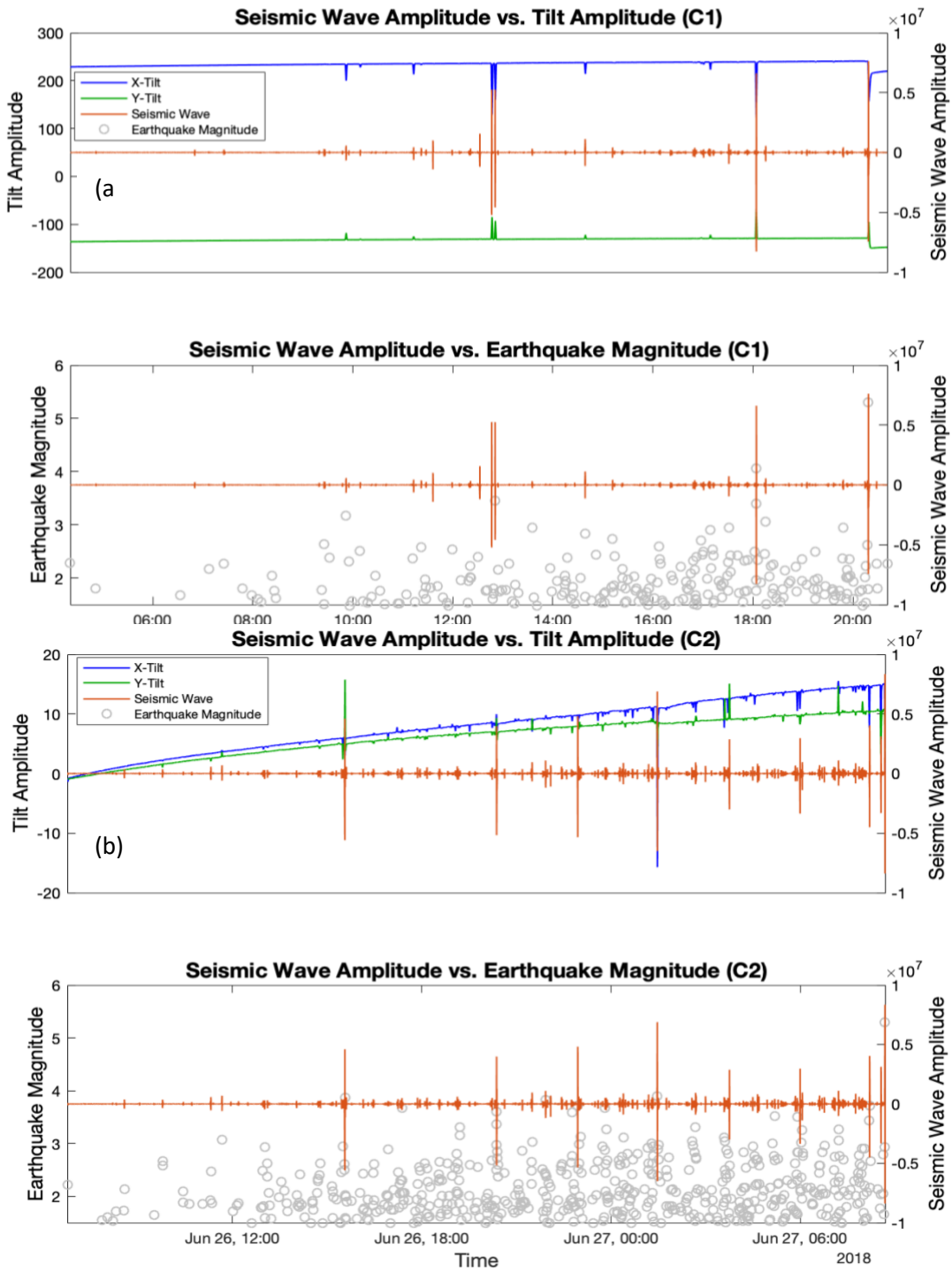

Figure 7. Correlation between seismic waveform (orange), X-tiltmeter data (blue), Y-tiltmeter data (green), and earthquake magnitude (gray circles). Top: Correlation between seismic waveform, X-tilt data and Y-tilt data. Bottom: Correlation between seismic waveform amplitude and earthquake magnitude. (a) Cluster C1 (June 16th 04:21:00 to 20:41:00 hours), last approximately 16:20:00 hours and includes 127 earthquakes. (b) Cluster C2 (June 26th 06:46:00 hours to June 27th 08:41:00 hours), lasted approximately 25:55:00 hours and includes 391 events.

Chapter 3: The Anatomy of the Cushing Fault Based on Earthquake Clustering and Crustal Reverberation

Introduction

The USA midcontinent has seen rapid increase in seismic activity and the state of Oklahoma has experienced the most significant earthquake rate increase, where the occurrence of seismic events exponentially increased from 2012 to 2015 (*Schoenball & Ellsworth, 2017*) and have slowly decreased since then. In Oklahoma, this increase in seismicity is mostly due to anthropological actives such as waste water disposal associated with oil and gas exploration (*Keranen et al., 2014; McGarr, 2014*); however, geological structures have a major influence on the spatial location of earthquakes sequences (*Shah & Keller, 2017; Pei et al., 2018*). Cushing, Oklahoma, is an interesting study area because a major oil and gas pipeline transportation system run through it (*McNamara et al., 2015*) and it has experienced a M5.0 sequence in November 2016 (*McGarr & Barbour, 2017*) and M4.3 sequence in October 2014 (*McNamara et al., 2015*).

Earthquakes within the M4.3 sequence are relatively shallow and in alignment with faults within the overlying Arbuckle group and the crystalline basement (*McNamara et al., 2015*). This sequence reactivated complex conjugate structures south of Cushing with a main fault striking WNW, which increased the likelihood of experiencing a larger event in the surrounding area (*McNamara et al., 2015*). The M5.0 earthquake sequence includes 48 earthquakes of M>3.0 and is considered as a continuation of the M4.3 sequence (*McGarr & Barbour, 2017*). The M5.0 sequence shiftted from the fault zone in 2014, and ruptured a previously unknown fault striking NE. The M5.0 sequence passed through the city limit of Cushing, and caused structural damage, but fourtunately, no damage to oil storage facilities (*McNamara et al., 2015; McGarr & Barbour, 2017*).

The Cushing fault zone has hosted some of the larger events in Oklahoma (e.g. M≥4 and M5.0 events), making it one of the major active fault zones in Oklahoma. For this reason, full characterization of the fault zone and improvements of the 1D velocity models in this area are essential to reduce uncertainties in earthquake locations, ground motion estimations, and to better understand controlling factors of large earthquake occurrences. In this study, we focus on constraining shallow structures, basement depth, and earthquake depths by combining waveform cross-correlation, identification and modeling of crustal reverberations.

Data

We use the earthquake catalog from OGS (Oklahoma Geological Survey) (*Walter et al., 2019*) for Cushing fault zone from June 2013 to July 2018, which includes 681 events with magnitudes from M0.25 to M5.0. About 95% of the events are located at depths between 0.1 km to 8.0 km (4.85%(8.01 – 86.3 km) and 95.15%(0.1 – 8.0 km)), with an average depth of 4.8 km. We downloaded event waveforms from IRIS (Incorporated Research Institutions for Seismology) DMC (Data Management Center) from 145 stations within 175 km of the fault zone. This resulted with a waveforms database consists of 16,031 P waveforms and 32,062 S waveforms. The waveforms are organized in GISMO waveform format (*Thompson and Reyes, 2018*). An auto-picker (*Li and Peng, 2016*) is applied to automatically pick P and S arrivals using a 1D velocity model for Cushing area extracted from the 3D model in *Chen (2016).* Based on the automatic phase picks, the waveforms are cropped into 4-second segments for P-waves, and 5.5-second segments for S-waves, each segment starting at -0.5 s of the picked arrival. The windowed waveforms are resampled to a uniform 100 Hz sampling rate. Seismicity in the Cushing fault zone is displayed on Figure 8.

Methods

Earthquake Cross-correlation

We measure waveform cross-correlation (CC) at each station for all possible event pairs after applying a Butterworth filter between 1 and 10 Hz to remove higher frequencies. Resampling is performed at peak CC to obtain more precise differential times using the GISMO package (*Thompson and Reyes, 2018*). We cluster event pairs with CC > 0.75 at each station for P and S waves.

Relative Double Difference Relocation

Differential times with CC values higher than 0.65 are used to obtain more precise relative locations using hypoDD (*Waldhauser, 2001*). The absolute location may shift depending on the 1D velocity model used, however, more precise relative locations are important to understand the crustal reflection patterns. For the hypoDD relocation input files, we used 226,801 differential times from CC and 100,130 differential times from the auto-picker catalog. The minimum and maximum number of CC measurements per events pair are 3 and 142 respectively. For the auto-picker catalog, we only include picks that have a signal to noise ratio (SNR) greater than 2.5 and we only consider events that are recorded at least at four stations. We performed five sets of iterations, specifications can be found on Table 1. After the CC and auto-picker catalogs differential time matched, we perform the relocation with 581 initial trial sources recorded at 174 seismic stations. The vp/vs ratio used for the relocation is vp/vs = 1.69 in the sedimentary layer. A nine layers 1D velocity model based on *Darold et al., (2015)* adapted for the Cushing area, with a shallower top layer is used. The velocity model can be found on Table 2.

Event Clustering

We refine our previously grouped events by only considering event pairs with CC > 0.85 and group them into high-quality clusters based on waveform similarity. For P waves, we only use the vertical channels and require at least 7 events with CC > 0.85 to form a high-quality cluster. For S waves, we use the two horizontal channels separately and require at least 5 events to form a high-quality cluster. Finally, we stacked the events and obtain the stacked waveform for each high-quality cluster.

Crustal Reverberations Detection

Visual examination of selected stations found multiple phases following the initial P and S arrivals. Previous studies suggests that these phases are likely caused by crustal reverberation within the sedimentary layer (*Mori, 1991*). A detection algorithm is developed to detect crustal reverberations in both vertical (P-wave) and horizontal (S wave) channels separately. To reduce random noise, the detection is performed on stacked waveforms for each cluster at each station. Only seismic stations that record two or more clusters with CC > 0.85 are considered for furthers steps. To detect crustal reverberations, we first divided the previously stacked waveforms of each sub-cluster into two signals: *Signal Prime* and *Signal Analysis*. For vertical channels, *Signal Prime* is defined as the first 0.35 seconds of data after P-wave arrival. For horizontal channels, *Signal Prime* is defined as the first 0.4 seconds of data after the S-wave arrival. *Signal Analysis* is defined as the data contained between *Signal Prime* and the end of the waveform data for both P and S waveforms. Finally, we compute a running correlation between *Signal Prime* and *Signal Analysis* to identified crustal reverberations (multiples) for individual channels based on absolute correlation coefficients (CC > 0.85). To improve the detection of subsequent arrivals, an envelope function based on Hilbert transform was implemented to obtain more precise parameters by

accounting for the phase shifts from reflection as described by *Hill, (1974)*. When all crustal reverberations are identified, we systematically measure and store the relative delay time and amplitude difference between the crustal reverberations for all clusters in individual channels separately.

Results

HypoDD relocation

The HypoDD relocated catalog for the Cushing Fault Zone includes 567 events with magnitudes from M0.3 to M5.0. The catalog event depths range from 0.1 km to 8.3 km, with an average depth of 2.2 km. HypoDD relocation results for Cushing sequence can be found on Figure 9. Clusters C1, C2 and C3 are randomly located in the original OGS catalog (Figure 9a,d), but they show a preferred earthquake depth distribution on the relocated catalog (Figure 9e). However, there is not a clear earthquake relocation along the fault zone (Figure 9b). Comparison between the original OGS catalog and the relocated catalog suggests significant improvement in delineating the fault zone (Figure 9b) and relative earthquake depth distribution (Figure 9e).

Similar event clusters

Based on waveform similarity and relative depth determination we detected similar event clusters at twelve different stations located between 30 km to 106 km from the Cushing seismic sequence. At each station we identify between two to three clusters, where each cluster is confined within narrow depth ranges (Figure 9e). The spatial distribution of these clusters confirms the accuracy of the relative depth determination of our relocation results.

Characteristics of crustal reverberations

We identify crustal reverberations in vertical channels at nine stations (RH07, RH11, STN01, STN02, STN03, STN07, STN08, STN20, and STN33) and in horizontal channels at five stations (STN03, STN09, STN15, STN31, and STN33). Station STN03 shows crustal reverberations in all channels (HH1, HH2, and HHZ) and station STN33 shows crustal reverberations in the vertical and one horizontal channel (HH1).

Each individual station has between two and three clusters, where each cluster is confined within narrow depth ranges. These clusters show at least one crustal reverberation (two peaks) and up to three crustal reverberations (four peaks). In this case, the first peak always corresponds to the direct P-wave arrival or S-wave arrival for vertical and horizontal channels respectively, thus the delay time for the first peak is always zero (dt = 0) and the amplitude ratio is always 1 (Amp. ratio = 1). Complete crustal reverberations parameters for vertical channels are listed on Table 3 and for horizontal channels on Table 4.

Figures 10 and 11 show examples of three similar event clusters grouped by waveform similarity on the vertical (HHZ) and horizontal (HH2) channels on station STN03. For both channels, the three clusters are confined within narrow depth ranges at shallow (~1.70 km), intermediate (~2.00 km), and deep (~2.60 km) depths. However, there is no clear location separation along the fault zone for these clusters. Figures 10c-d and 11c-d show velocity and displacement waveforms of the stacked P-wave and S-wave for the three clusters, respectively.

Figures 12 and 13 show other examples of three similar event clusters on the vertical (HHZ) channel and two similar event clusters on horizontal (HH2) channel group by waveform similarity on station STN33. For both channels, the shallow and deep clusters are confined within narrow depth ranges at 1.65 km and 2.42 km respectively. The intermediate cluster on the vertical channel

is confined within a narrow depth range around 1.86 km. Similarly, to station STN03, the clusters on station STN33 do not show clear location separation along the fault zone. Figures 12c-d and 13c-d show velocity and displacement waveforms of the stacked P-wave and S-wave clusters respectively. For stations STN03 and STN33, it can be noted that the delay times between successive reverberations are very similar for the three clusters at different depths, despite slight delay of the deepest cluster. The main difference is the relative amplitude of the reverberations: the shallowest clusters have strongest reverberation signal, which can have higher amplitude than the direct P/S arrivals. Clusters at intermediate and deeper depths have similar amplitude ratios, despite slight lower amplitude for reverberations from the deepest clusters.

Figure 14a shows a map view of all stations that recorded crustal reverberations on one or more channels. Figure 14b and 14c show the stacked waveform of all observations for P wave clusters and S wave clusters respectively. P wave clusters are detected at stations located between 30 km to 104 km from the seismic sequence (Figure 14b). S wave clusters are detected at stations located between 35 km to 66 km from the seismic sequence (Figure 14b). Our observations suggest nearly constant delay time between crustal reverberations across wide distance ranges.

Discussion

The strong spatial clustering of similar event clusters from multiple stations suggests that reliability of the double-difference relocation performed in this study (*Waldhauser*, 2001). If only differential times from cross-correlation are used in relocation, the largest earthquakes (M≥4) are excluded from the relocation due to lack of waveform similarity with smaller events. With high-quality picks from the auto-picker, the relocation successfully relocated the M4.3 and M5.0 events within the Cushing fault zone (Figure 15).

The presence of crustal reverberations in this area is caused by free surface reflections at the interface between the low-velocity sedimentary layer and the high-velocity crystalline basement *(Frohlich et al., 2014)*. Similar observations made in Texas, California, and the New Madrid seismic zone *(Mori, 1991; Langston, 2003; Frohlich et al., 2014)* suggest the possibility of using crustal reverberations to constrain earthquake depth and shallow structures depth. In this study, we use a systematically technique that combines crustal reverberation analysis and cross-correlation to calculate earthquake depths relative to the basement interface for earthquake clusters. This systematically technique is transferable to other earthquake sequences in Oklahoma (e.g. Prague, Guthrie, Fairview, etc.) and nearby regions in the central US such as Kansas, Texas, and New Madrid seismic zone.

The relative amplitude variations of crustal reverberations (Figure 10-11) are clear evidence that events with different source depths have different waveform characteristics. Although, the direct P-wave or S-wave arrivals are similar, the full waveforms have different behavior. Proper modeling needs to be done to accurately identify the amplification or attenuation parameters of the seismic waveforms, especially of the crustal reverberations. The relative timing and amplitude variations of the crustal reverberations can be used to constrain earthquake depth with the implementation of forward modeling (*Mori, 1991; Frohlich et al., 2014*). Determining accurate absolute event depth is a key factor for ground motion modeling and to understand the triggering mechanism of events by proper identification of the seismogenic zone.

The HypoDD relocated catalog for the Cushing Fault Zone includes 567 events with magnitudes from M0.3 to M5.0. The catalog event depths range from 0.1 km to 8.3 km, with an average depth of 2.2 km. The relocated catalog suggests significant improvement in delineating

the fault zone and relative depth relocation, where the relocated clusters show a preferred depth distribution. Shallow event clusters are found near a narrow dipping surface, which may be an erosional surface at basement interface. Based on our double-difference relocation results and preferred earthquake depth cluster distribution (Figure 9e), we suggest that the dipping basement interface may range from 1.6 km to 2.0 km.

Observations in Figures 10-13 suggest that the delay time may not change much for clusters located at different depth. However, the relative amplitude changes significantly between the shallowest and deeper depths. Forward waveform modeling suggests that the delay time is mainly related to basement depth and shallow velocity gradient, while the earthquake depth is the main control on relatively amplitudes of crustal reverberation. The strong reverberation amplitude and the narrow depth range of the shallowest cluster suggest that it occurs directly beneath the basement interface.

The relative amplitude variations of crustal reverberations (Figure 10 - 13) are clear evidence that events with different source depths have different waveform characteristics. Although the direct P-wave or S-wave arrivals are similar, the full waveforms have different behavior. The relative timing and amplitude variations of the crustal reverberations can be used to constrain earthquake depth with the implementation of forward modeling (*Mori, 1991; Frohlich et al., 2014*). The analysis that combines crustal reverberation and cross-correlation to constrain earthquake depths relative to the basement interface for earthquake clusters can be transferable to other earthquake sequences in Oklahoma (e.g. Prague, Guthrie, Fairview, etc.) and nearby regions in the central US such as Kansas, Texas, and New Madrid seismic zone.

These multiple reverberations may cause multiple shaking reports for the same earthquake, and the stronger amplitudes for later arrivals for shallow events can cause problem for ground

motion modeling. In addition, because the delay time for the same fault zone only shows very little variations with source-receiver distance, the later arrivals could be regarded as separate events occurring at regular intervals, which can cause problem for earthquake sequence analysis (e.g. multiple events occurring at regular intervals versus just a single event). The identification of shallow events potentially directly below the basement interface is very important to understand fluid pathways from injection wells to fault zone. The analyses here underscore the importance for accurate depth determination and shallow structure in both hazard assessment and earthquake triggering.

Conclusion

We use a technique that systematically combines crustal reverberation and cross-correlation to better understand waveform behavior and characteristics for groups of events at different depths in the Cushing fault zone. This technique and the implementation of forward modeling can be used to constrain shallow structures depths and earthquake depths relative to the basement interface. This technique is transferable to nearby regions in Oklahoma and the central USA. In the crustal reverberations analysis, we study the relative time and amplitude variations between crustal reverberations for clusters confined within narrow depth ranges. The relative timing between crustal reverberations is consistent for clusters at different depths, however the relative amplitude of the crustal reverberations varies with source depth. The shallower depth cluster (C1) shows stronger reverberation arrivals than intermediate and deeper depth clusters. We identify crustal reverberations in the vertical channel at nine stations and at five stations in horizontal channels. Individual stations present between two to three clusters with different depth

sources, and each cluster presents between one to three reverberations after the direct P-wave or S-wave arrivals.

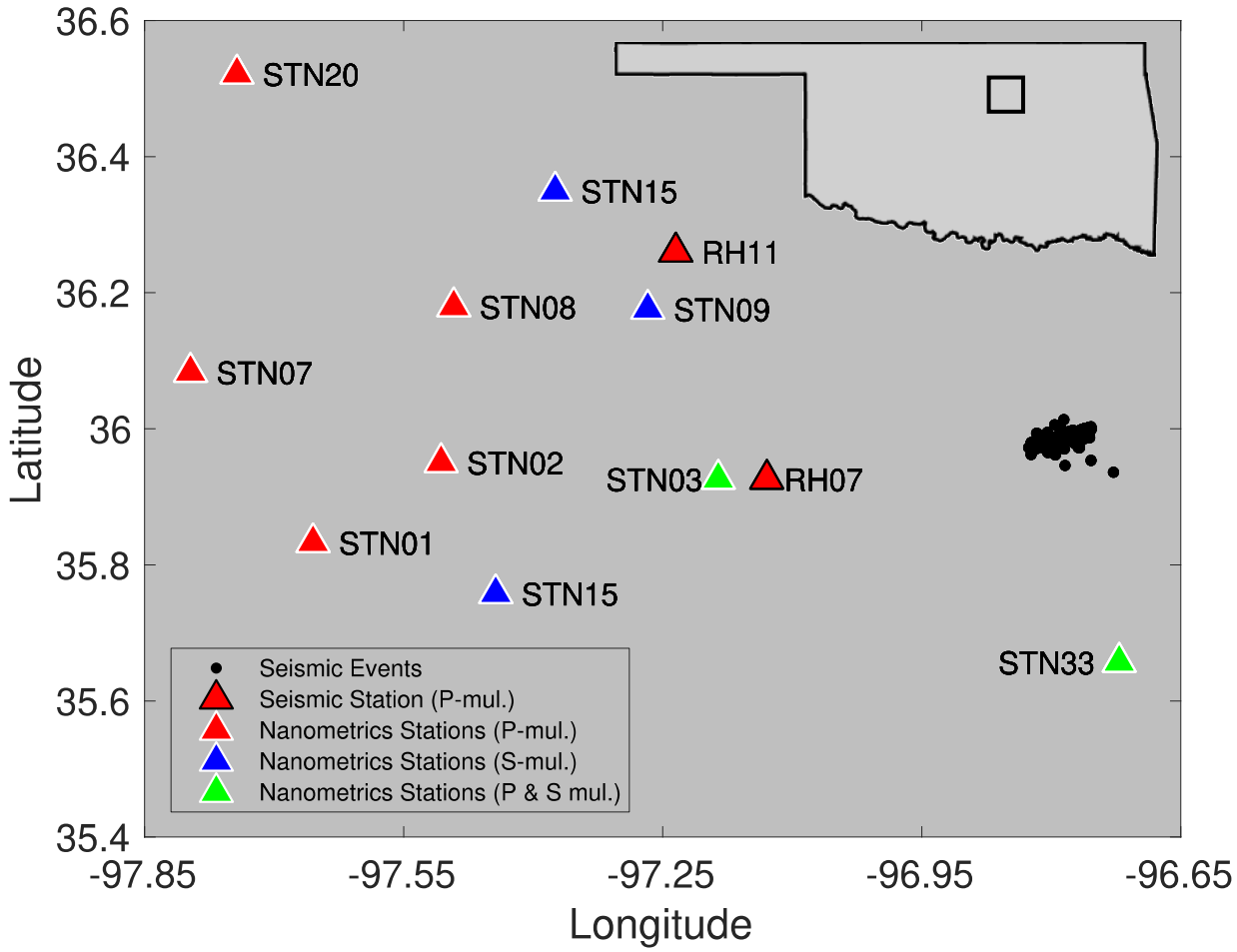

Figure 8. Map view of the study area. Cushing Fault Zone events (black dots) and stations that recorded crustal reverberations in one or more channel (triangles). The color of each station corresponds to the type of crustal reverberations (multiples) recorded: P multiples (red), S multiples (blue), P and S multiples (green). The outline color of each station corresponds to the type of recording station: seismic stations (black) or nanometric stations (white).

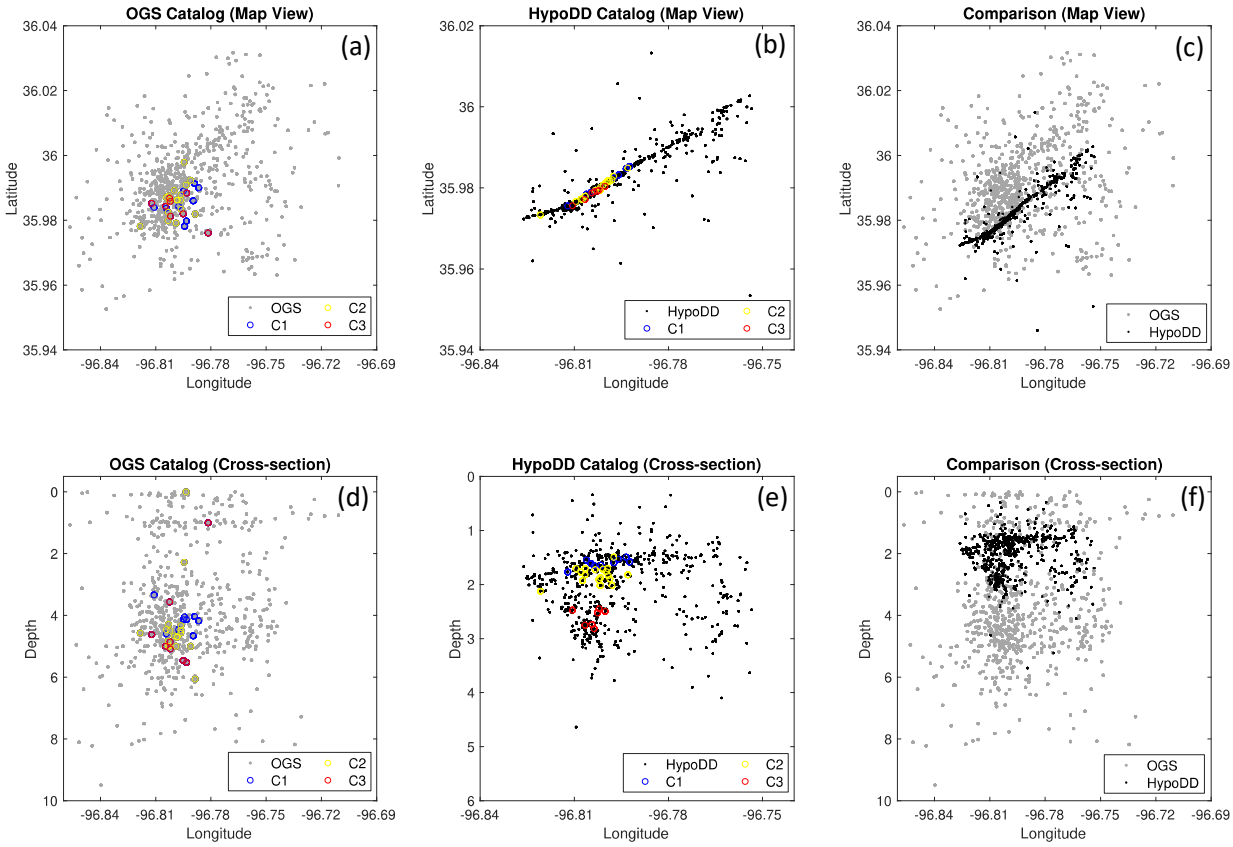

Figure 9. Comparison between the original Oklahoma Geological Survey (OGS) catalog (gray dots) and the double-difference relocated (HypoDD) catalog (black dots). Similar cluster events at station STN03, C1 – shallow cluster (blue circles), C2 – intermediate cluster (yellow circles), and C3 – deep cluster (red circles). (a) OGS catalog map view. (b) HypoDD catalog map view. (c) Map view comparison between OGS and HypoDD catalogs. (d) OGS catalog cross-section view. (e) HypoDD catalog cross-section view. (f) Cross-section view comparison between OGS and HypoDD catalogs.

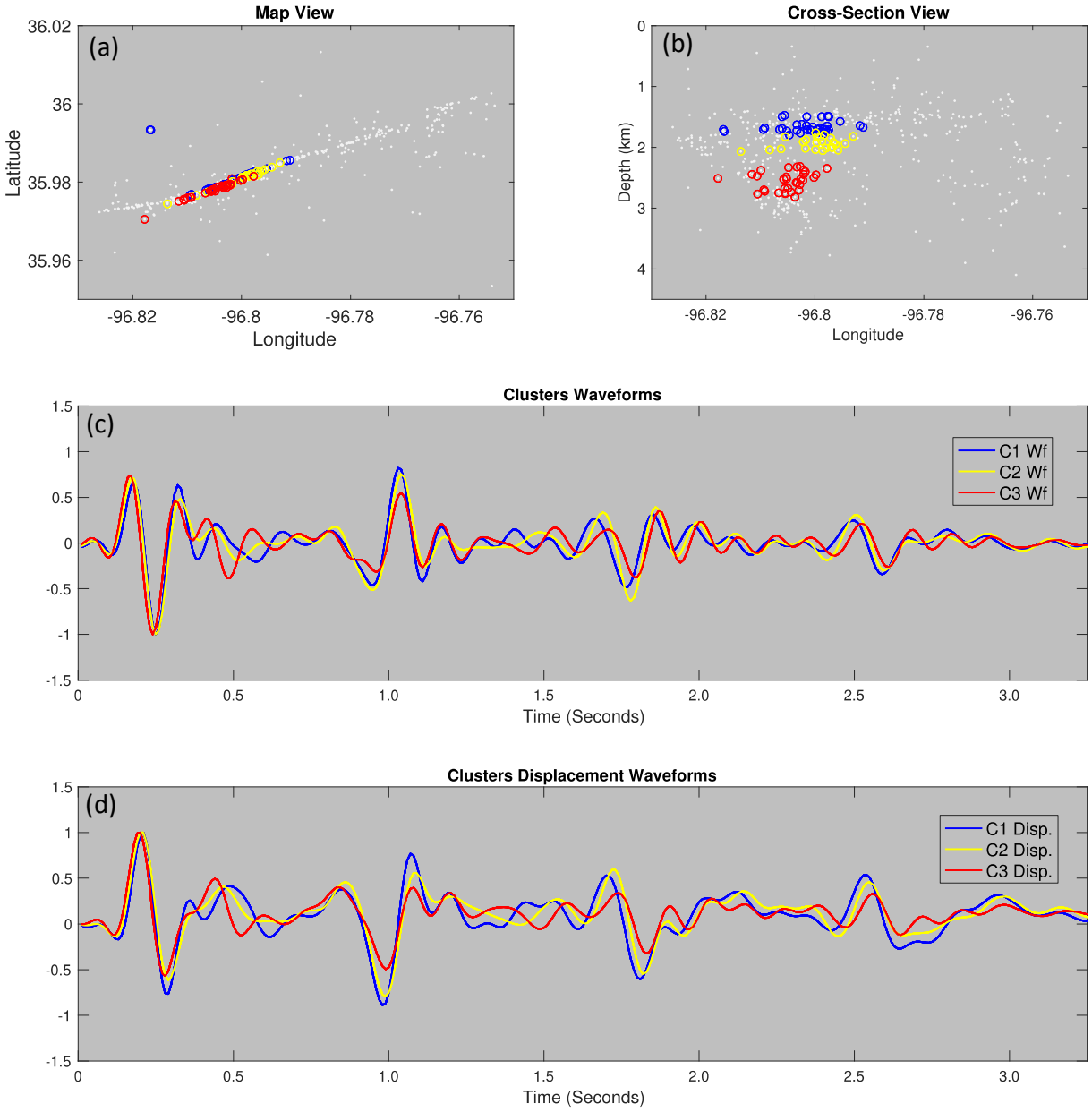

Figure 10. Crustal reverberations on vertical channel (HHZ) at station STN03 for three clusters: C1- shallow depth cluster (blue), C2- intermediate depth cluster (yellow), and C3- deepest depth cluster (red). (a) Map view of C1, C2, and C3 in the Cushing Fault Zone. (b) Cross-section view of C1 (located around 1.60 km), C2 (located around 1.82 km), and C3 (located around 2.61 km). We suggest a dipping basement interface ranging from 1.6 km to 2.0 km. (c) Stacked waveforms for C1 (blue waveform), C2 (yellow waveform), and C3 (red waveform). (d) Stacked displacement waveforms for C1 (blue waveform), C2 (yellow waveform), and C3 (red waveform).

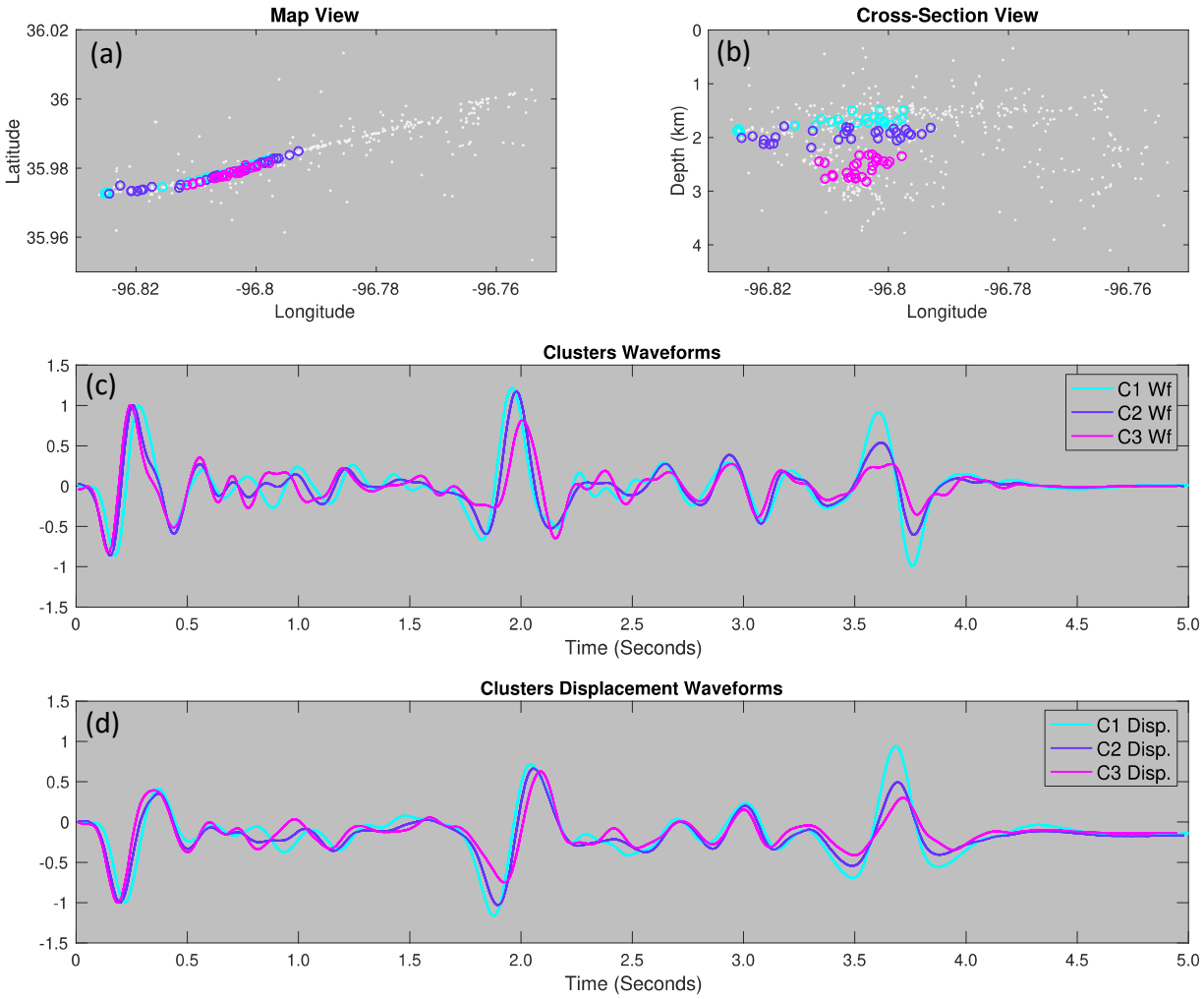

Figure 11. Crustal reverberations on horizontal channel (HH2) at station STN03 for three clusters: C1- shallow depth cluster (cyan), C2- intermediate depth cluster (purple), and C3- deepest depth cluster (magenta). (a) Map view of C1, C2, and C3 in the Cushing Fault Zone. (b) Cross-section view of C1 (located around 1.68 km), C2 (located around 1.91 km), and C3 (located around 2.80 km). We suggest a dipping basement interface ranging from 1.6 km to 2.0 km. (c) Stacked waveforms for C1 (cyan waveform), C2 (purple waveform), and C3 (magenta waveform). (d) Stacked displacement waveforms for C1 (cyan waveform), C2 (purple waveform), and C3 (magenta waveform).

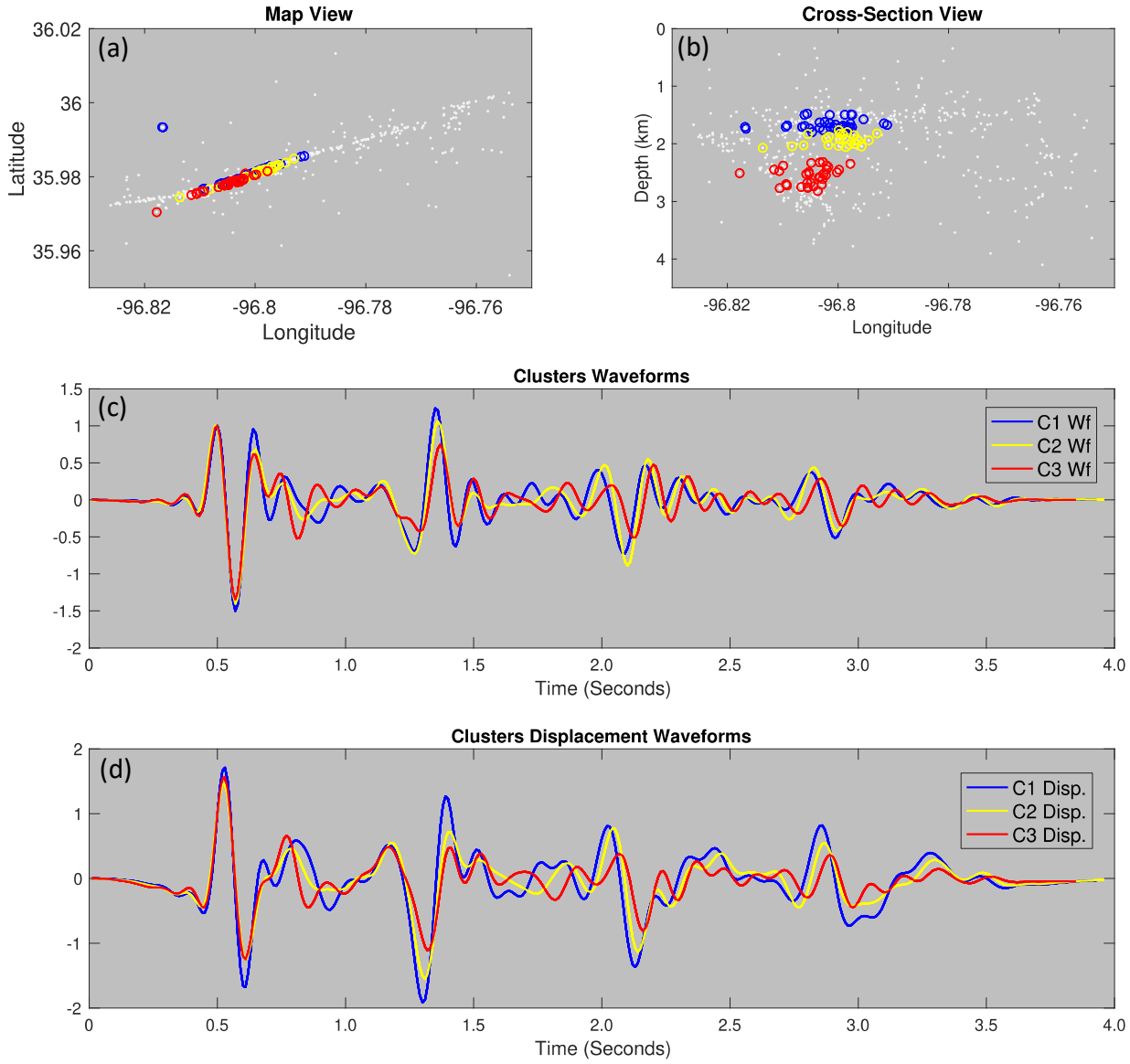

Figure 12. Crustal reverberations on vertical channel (HHZ) at station STN33 for three clusters: C1- shallow depth cluster (blue), C2- intermediate depth cluster (yellow), and C3- deepest depth cluster (red). (a) Map view of C1, C2, and C3 in the Cushing Fault Zone. (b) Cross-section view of C1 (located around 1.64 km), C2 (located around 1.86 km), and C3 (located around 2.44 km). We suggest a dipping basement interface ranging from 1.6 km to 2.0 km. (c) Stacked waveforms for C1 (blue waveform), C2 (yellow waveform), and C3 (red waveform). (d) Stacked displacement waveforms for C1 (blue waveform), C2 (yellow waveform), and C3 (red waveform).

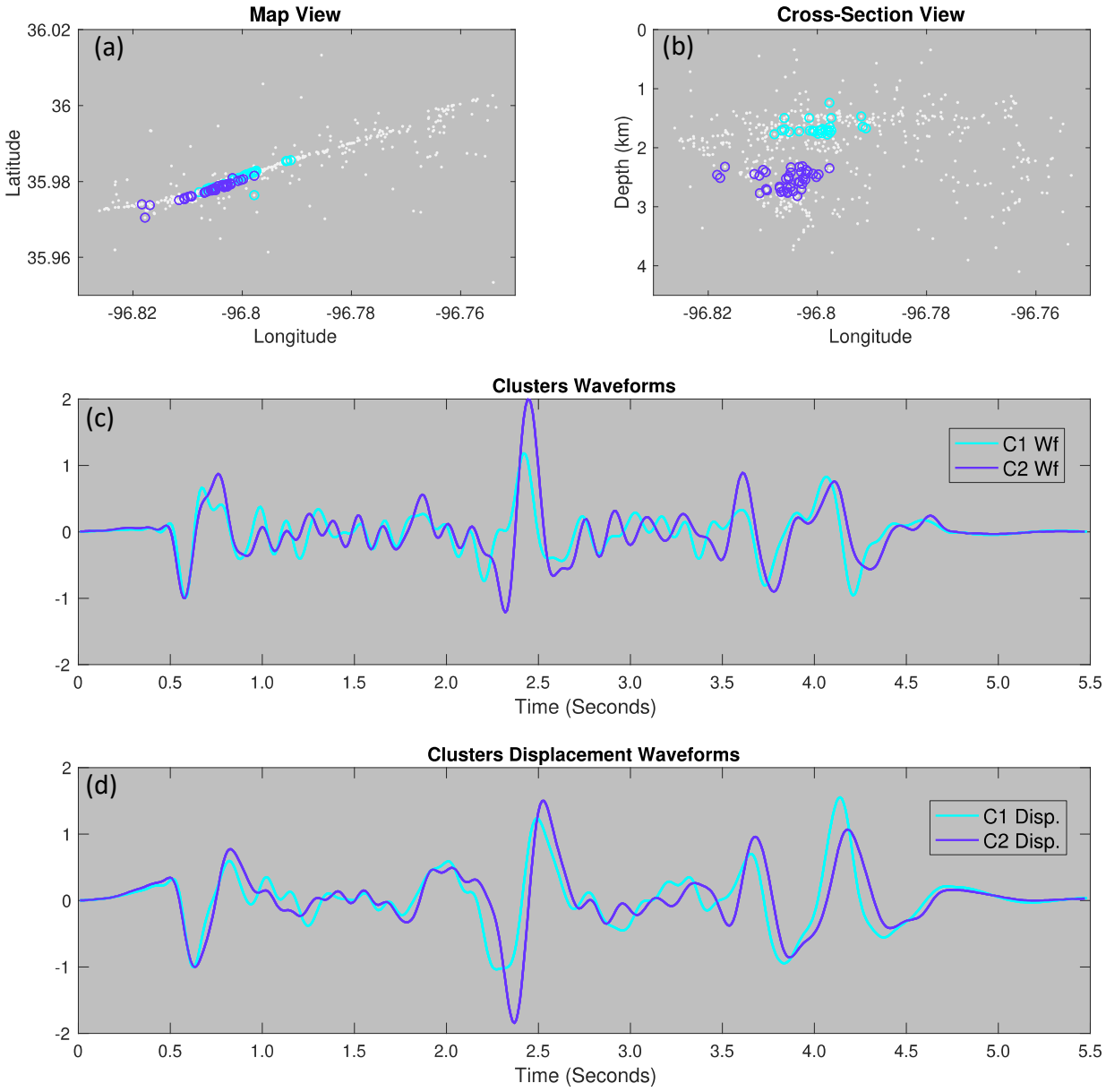

Figure 13. Crustal reverberations on horizontal channel (HH1) at station STN33 for two clusters: C1- shallow depth cluster (cyan) and C2 - deep depth cluster (purple). (a) Map view of C1and C2 in the Cushing Fault Zone. (b) Cross-section view of C1 (located around 1.66 km) and C2 (located around 2.41 km). We suggest a dipping basement interface ranging from 1.6 km to 2.0 km. (c) Stacked waveforms for C1 (cyan waveform) and C2 (purple waveform). (d) Stacked displacement waveforms for C1 (cyan waveform) and C2 (purple waveform).

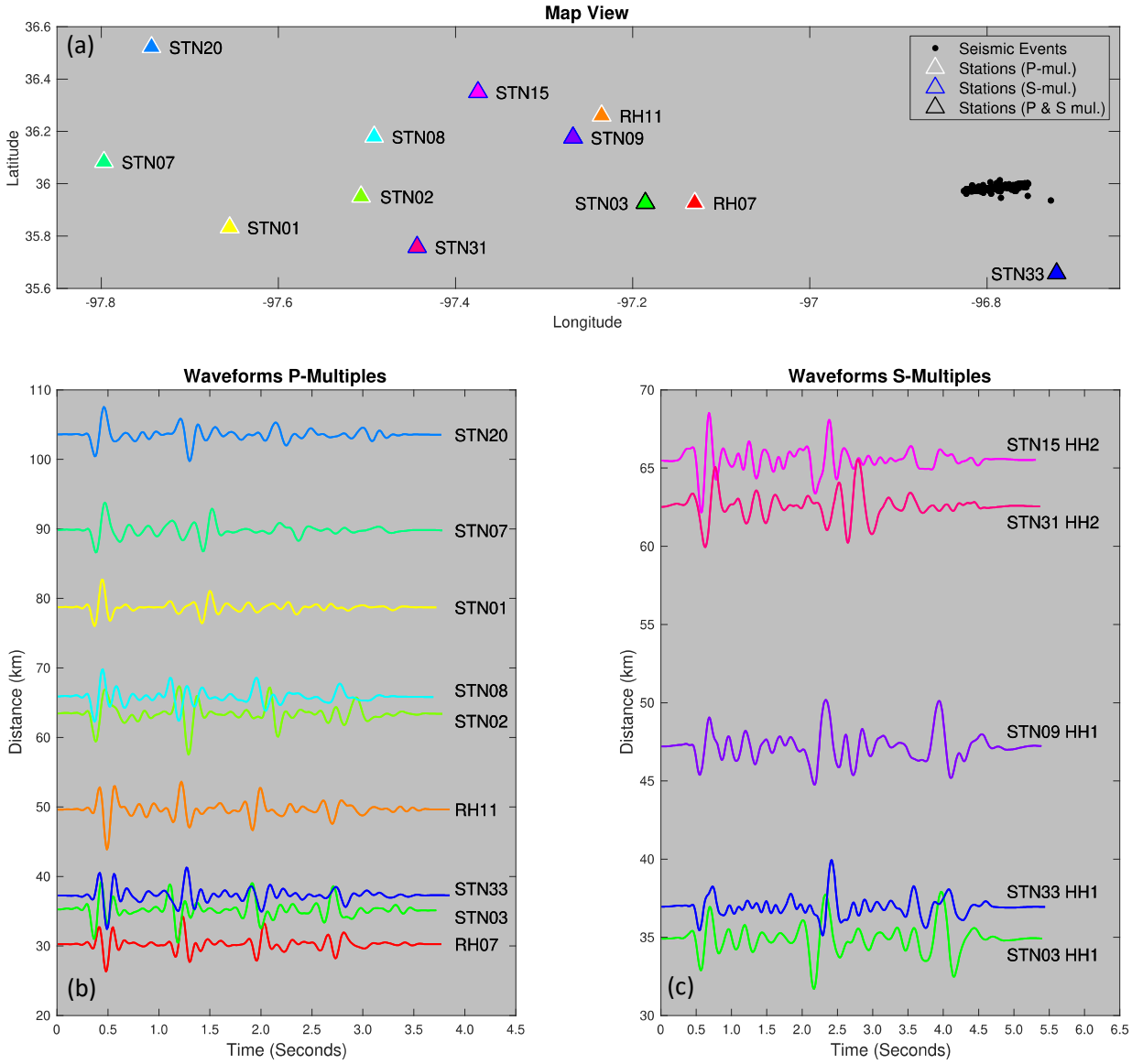

Figure 14. (a) Map view of stations in central Oklahoma that recorded crustal reverberations on one or more channels from the Cushing sequence (black dots). Stations that recorded P wave crustal reverberations (white outline), S wave crustal reverberations (blue outline), and P and S wave crustal reverberations (black outline). The color of each station corresponds to the color of waveform in panels (b) and (c). (b) Stacked waveforms for nine stations that recorded P wave crustal reverberations sorted by distance. (c) Stacked waveforms for five stations that recorded S wave crustal reverberations sorted by distance.

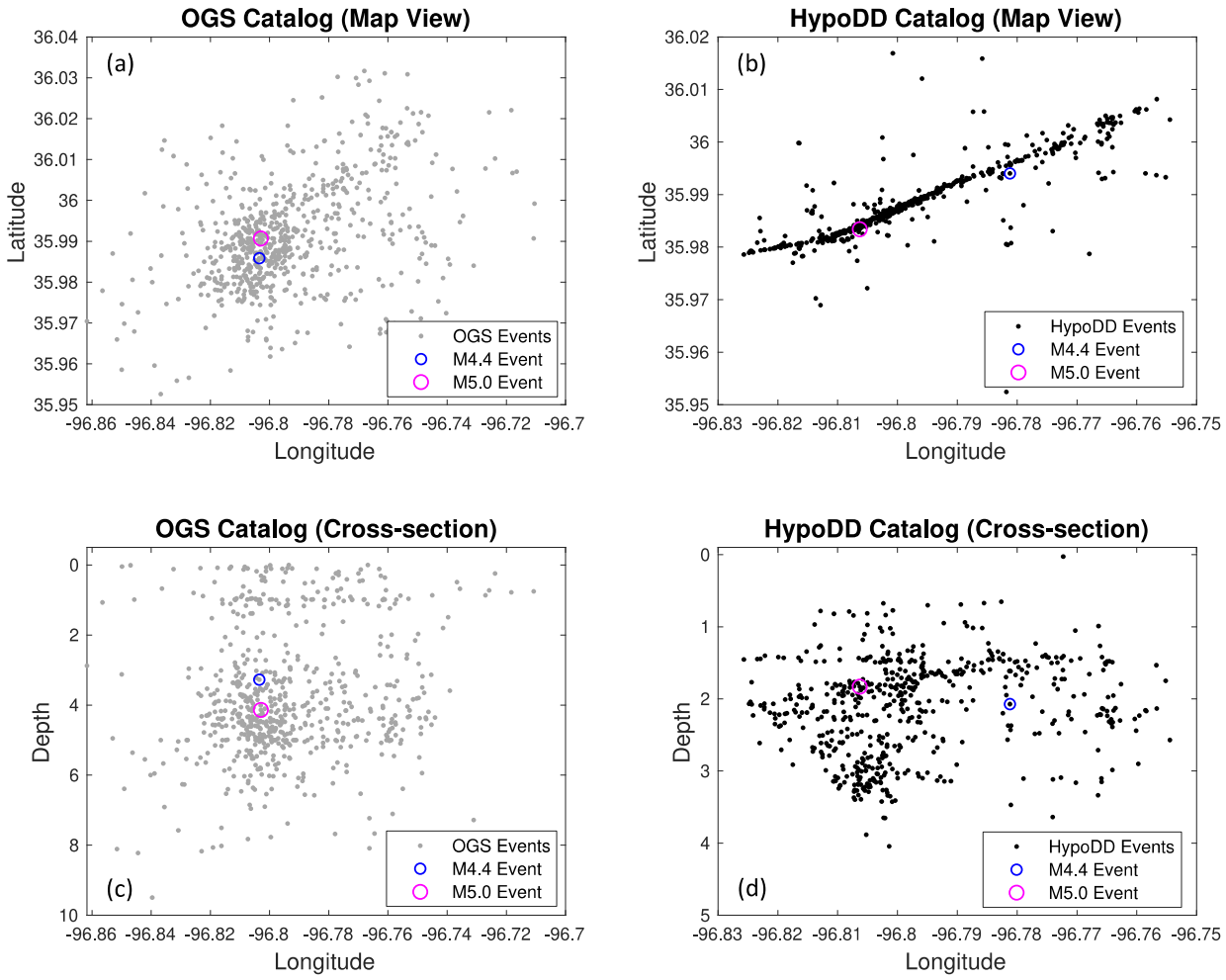

Figure 15. Oklahoma Geological Survey (OGS) catalog (red dots) and double-difference relocated (HypoDD) catalog (black dots) comparison for Cushing sequence and M4.4 event (blue circle) and M5.0 (magenta circle). (a) OGS catalog map view. (b) HypoDD catalog map view. (c) OGS catalog cross-section view. (d) HypoDD catalog cross-section view.

NITER*	WTCCP†	WTCCS‡	WRCC¶	WDCC§	WTCTP ‖	WTCTS#	WRCT**	WDCT††	DAMP‡‡
3	0.5	0.5	-9	-9	1	0.9	-9	-9	150
3	0.5	0.5	-9	-9	1	0.9	10	10	160
3	1	0.85	-9	5	0.85	0.65	10	10	170
3	1	0.75	8	8	0.75	0.35	6	6	180
5	1	0.65	7	10	0.1	0.005	5	5	190

Table 1. Iteration parameters for double difference relocation. * Last iteration to use the following weights †Weight P cross-correlation ‡ Weight S cross-correlation ¶ Weight P catalog § Weight S catalog ‖Residual threshold in seconds for cross-correlation data # Residual threshold in seconds for catalog data **Maximum distance in kilometers between cross-correlation linked pairs †† Maximum distance in kilometers between catalog linked pairs ‡‡Damping

LAYER #	1	2	3	4	5	6	7	8	9
TOP* (km)	0	0.3	1.0	1.5	8.0	21.0	42.0	50.0	80.0
VEL† (km/s)	2.50	2.95	4.15	5.80	6.27	6.41	7.90	8.15	8.50

Table 2. Nine-layer 1D velocity model for Cushing fault zone adapted from *Darold et al., (2015).* * Depth of top of layer †Velocity.

STA*	CHAN†	CLUS No‡	EPC¶	PN§	DELAY TIMES	AMP RATIO‖	AVE DEP#	AVE DIS**
RH07	EHZ	1	11	4	0;0.73;1.46;2.21	1,-1.05,1,1	1.81	31.17
RH07	EHZ	2	52	4	0;0.74;1.48;2.20	1,-1.04,0.73,0.42	1.89	30.36
RH07	EHZ	3	66	4	0;0.75;1.50;2.25	1,-0.94,0.72,0.40	2.17	30.27
RH11	EHZ	1	9	4	0;0.73;1.43;2.21	1,-0.75,0.81,0.92	1.90	49.65
RH11	EHZ	2	8	4	0;0.74;1.44;2.20	1,0.76,0.76,0.75	2.85	49.59
STN01	HHZ	1	22	2	0;1.06	1,0.96	1.55	78.72
STN01	HHZ	2	15	2	0;1.05	1,0.79	1.74	78.72
STN01	HHZ	3	17	2	0;1.06	1,0.64	1.99	78.66
STN02	HHZ	1	14	4	0;0.91;1.70;2.44	1,1.03,1.05,1.14	1.94	63.92
STN02	HHZ	2	21	4	0;0.91;1.67;2.44	1,1.02,-0.97,0.59	2.54	63.38
STN03	HHZ	1	9	4	0;0.74;1.48;2.23	1,-1.06,1.21,1.40	1.60	35.41
STN03	HHZ	2	18	4	0;0.75;1.50;2.25	1,-1.08,1.06,0.94	1.82	35.18
STN03	HHZ	3	7	4	0;0.76;1.57;2.21	1,-1.05,-1.09,0.83	2.61	35.01
STN07	HHZ	1	17	3	0;1.05;1.89	1,0.96,-1.08	1.73	89.80
STN07	HHZ	2	8	3	0;1.06;1.89	1,0.61,0.45	2.02	89.44
STN08	HHZ	1	19	4	0;0.75;1.60;2.30	1,-1.03,-1.06,1.14	1.66	65.83
STN08	HHZ	2	13	4	0;0.76;1.51;2.32	1,-1.01,0.88,0.81	1.91	65.95
STN08	HHZ	3	17	4	0;0.78;1.56;2.33	1,-0.83,0.67,0.45	2.57	65.58
STN20	HHZ	1	8	3	0;0.81;1.64	1,-0.99,1.04	1.65	103.52
STN20	HHZ	2	11	3	0;0.84;1.70	1,-0.97,0.83	1.91	103.55
STN33	HHZ	1	39	4	0;0.78;1.50;2.20	1,-0.90,1.06,1.14	1.64	37.29
STN33	HHZ	2	26	4	0;0.79;1.53;2.34	1,-0.96,0.92,0.93	1.86	37.19
STN33	HHZ	3	34	4	0;0.80;1.55;2.25	1,-0.85,0.50,0.36	2.44	36.95

Table 3. Crustal reverberations parameters in vertical channels. *Seismic station †Channel ‡Cluster number ¶Number of earthquakes per cluster §Number of peaks ||Amplitude ratio #Average depth in kilometers, rounded to the nearest hundredths **Average distance in kilometers, rounded to the nearest hundredths.

STA*	CHAN†	CLUS No‡	EPC¶	PN§	DELAY TIMES	AMP RATIO‖	AVE DEP#	AVE DIS**
STN03	HH1	1	35	3	0;1.59;3.36	1,1.06,-1.02	1.68	34.91
STN03	HH1	2	18	3	0;1.82;3.33	1,-0.82,-0.64	1.91	35.35
STN03	HH2	1	23	3	0;1.65;3.37	1,1.12,-0.99	2.80	34.81
STN03	HH2	2	31	3	0;1.75;3.30	1,1.10,0.74	2.05	34.68
STN03	HH2	3	28	3	0;1.80;3.26	1,0.84,-0.40	2.60	34.97
STN09	HH1	1	15	3	0;1.60;3.20	1,-1.04,1.14	1.70	47.18
STN09	HH1	2	8	3	0;1.98;3.58	1,-1.02,-0.87	1.95	47.25
STN15	HH2	1	23	2	0;1.81	1,-0.99	1.67	65.53
STN15	HH2	2	19	2	0;1.83;	1,-0.84	1.86	65.61
STN31	HH2	1	28	2	0;2.44	1,1.09	1.73	62.66
STN31	HH2	2	33	2	0;2.33	1,-0.77	1.90	62.56
STN31	HH2	3	9	2	0;1.80	1,0.75	2.57	62.85
STN33	HH1	1	26	3	0;2.05;3.17	1,-1.08,-1.14	1.66	37.24
STN33	HH1	2	45	4	0;1.98;3.24	1,-1.03,-0.94	2.41	36.94

Table 4. Crustal reverberations parameters in horizontal channels. *Seismic station †Channel ‡Cluster number ¶Number of earthquakes per cluster §Number of peaks ||Amplitude ratio #Average depth in kilometers, rounded to the nearest hundredths **Average distance in kilometers, rounded to the nearest hundredths

Chapter 4: Spatially Distinct Tectonic Zones Across Oklahoma Inferred from Shear Wave Splitting

Introduction

The U.S. midcontinent, especially Oklahoma and southern Kansas, has experienced significant seismicity rate changes over the last decade, where the number of seismic events dramatically (not necessarily exponentially) increased from 2009 until 2016, and has slowly decreased since end of 2016 (*Schoenball & Ellsworth, 2017; Walter et al., 2019*). These fluctuations in seismicity are linked to the significant amount of wastewater that were disposed into the Arbuckle formation, which overlies the crystalline basement in Oklahoma and southern Kansas (*Ellsworth, 2013; Walsh & Zoback, 2015; Schoenball & Ellsworth, 2017*). Many of the earthquake sequences occur due to reactivation of pre-existing structure. However, in some cases, the network geometry is unfavorable to map fault structures and dominant stress orientations in the region, which limits our understanding of the driving mechanism of earthquake sequences (*Schoenball & Ellsworth, 2017*). In this study, we perform shear wave splitting analyses on individual stations to better understand regional shear wave polarization that may be caused by underlying geologic structures and regional stresses.

When a shear wave encounters an anisotropic medium, it can split into two orthogonally polarized quasi-shear waves (*Crampin, 1984*), with one wave arriving first with faster velocity, and the second wave arriving later with slower velocity and orthogonal to direction of the faster shear wave. There are two shear wave splitting parameters that help quantify the anisotropy in the medium: delay time (δt) and fast polarization direction (ϕ). The delay time (δt) represents the difference in arrival time between the fast and slow shear waves, the delay time (δt) is proportional to the percentage of anisotropy in the medium. The fast polarization direction (ϕ) is the angle

between the fast and slow shear waves, it also reflects the orientation of the structure that is causing the anisotropy in the area. Shear wave splitting parameters are mostly used for monitoring stress changes (*Savage et al., 2010; Unglert et al., 2011; Johnson & Savage, 2012*), to explore possible earthquake prediction (*Castellazzi et al., 2015*), and to map fracture networks *(Verdon et al., 2009; Gao et al., 2011; Wuestefeld et al., 2011; Baird et al., 2013*).

In this study, we used an automatic shear wave splitting (SWS) technique *(Savage et al., 2010)* to measure SWS parameters (fast direction [ϕ] and delay time [δt]). We also execute a spatiotemporal analysis of the fast direction of polarization (ϕ) in Oklahoma and Southern Kansas, and compare with other datasets to better understand the control factors of seismic anisotropy and relationship with geological structure.

Data

We use the Oklahoma Geological Survey (OGS) earthquake catalog (*Walter et al., 2020*) to calculate shear-wave splitting parameters. The earthquake catalog includes 33,367 events in Oklahoma from January 2010 to September 2019. The events range in magnitude from M 1.0 to M 5.8 and in depth from 0 to 45.25 kilometers, with an average depth of 8.87 kilometers. The map view of the seismicity is displayed on Figure 16. The earthquakes are recorded by 247 seismic stations from the Oklahoma Seismic Network (OK), the Oklahoma Consolidated Temporary Seismic Network (O2), the US Geological Survey Network (GS), and other stations.

Method

To calculate the shear wave splitting parameters, the fully automated software MFAST (Multiple Filter Automatic Splitting Technique) was used. The MFAST software filters the data,

calculates the signal to noise ratio (SNR), and finally calculates the shear-wave splitting parameters, including the time delay between the original and split waves (δt) and fast direction of polarization (ϕ). The only manual step of this software is to pick the P and S arrival times.

The MFAST tool uses a combination of the minimum energy and the Eigenvalue techniques developed by *Silver and Chan (1991),* and implements a cluster analysis on multiple measurement windows to determine the best results (*Savage et al., 2010*). Multiple bandpass filters are used to find the best signal and frequency bands for parameter calculations. Broader bandpass filter is preferred over narrow bandpass filter, because the latter may cause cycle skipping problems (*Savage et al., 2010*). For each event, the optimal bandpass filter is determined from a set of 14 predefined bandpass filters based on the signal to noise ratio (SNR) and the width of the filter.

The signal to noise ratio (SNR) is calculated for the filtered data using the same window length for the signal and noise (~7 seconds). The signal window starts immediately after the S wave arrival and the noise window ends immediately before the S wave arrival. The ratios of the root mean square (rms) between the signal amplitude and the noise amplitude from the north and east components are averaged to calculate the signal to noise ratio (SNR) (*Savage et al., 2010*). Measurements that are below the predefined minimum signal to noise ratio (SNR < SNRmax, usually equals 3), are not considered at the time of interpretation. If more than one filter gives the same signal to noise (SNR) value, the measurement that is most stable with frequency will be chosen as the final measurement.

The minimum energy method can only be successfully applied when the polarization of the incoming waves is known (SKS and SKKS waves). On the other hand, the Eigenvalue method can be used when the polarization is unknown but this technique is very susceptible to noise, so it

can provide less accurate splitting parameters in comparison to other splitting techniques like the cross-correlation method (*Fukao, 1984*). Since the MFAST software uses a combination of the minimum energy and Eigenvalue methods, the resulted parameters give the best approximate solution for shear wave splitting parameters.

Results

We obtained 524,395 shear wave splitting measurements from MFAST software. To ensure the reliability of subsequent analysis, we constrain the results by applying a quality control factor. We follow previous studies (*Savage et al., 2010; Rafayee et al., 2014; Li & Peng, 2017*) and define high-quality measurements by (1) A-grade cluster; (2) delay time (δt) < 0.2 seconds, since we are only working with local seismicity; (3) fast direction error (f_err) < 10°; (4) delay time error (δt_err) < 0.05 seconds; (5) signal to noise ratio (SNR) > 3; and (6) epicentral distance (Δ) < 25 kilometers. After applying these thresholds, we have 7,916 high-quality measurements at 35 stations for localized seismicity. However, when we defined high-quality measurements for regional seismicity (epicentral distance (Δ) < 150 kilometers), we obtain 384,325 high-quality measurements.

We display all stations that have more than 100 high-quality measurements in Oklahoma and southern Kansas in Figure 16. To illustrate sub-regional variations and the influence of data quality control, especially the effect of epicentral distance control, we present SWS results for localized (Figure 17) and regional (Figure 18) seismicity. We isolate eight representative stations in four distinct regions of the study area: (1) southern Kansas: KAN01 and KAN10; (2) Fairview area, located in northwestern Oklahoma: FW06 and OK039; (3) Pawnee area, located in northeastern Oklahoma: PW11 and PW14; (4) central Oklahoma: FNO and SMO. The spatial

distribution of the stations with reliable results provides adequate coverage to identify spatial patterns of anisotropy in this region over the last nine years.

The SWS-determined fast direction of polarization (ϕ) for localized seismicity is shown on Figure 17a for localized seismic and on Figure 18a for regional seismicity. Contrary to other SWS studies (*Nolte et al., 2017*), we did not observe time varying fast polarization directions (ϕ). However, we find the peculiar characteristic that at most stations, we observe the presence of two predominant directions of fast polarization as seen on *Cochran et al., (2020)*. These fast polarization directions, primary (ϕ_{pri}) and secondary (ϕ_{sec}), are defined at each station by finding the local maxima (peaks) among the SWS-measured values. To find these peaks, the MATLAB function *findpeaks* is used. The primary fast polarization direction is defined as the most prominent peak, and the secondary fast polarization direction is defined as the second most prominent peak that is also found at least 30 degrees away from the primary peak. If there is just one peak (global maxima) detected on the dataset, then this station will only have a primary fast direction of polarization.

The thicker black line represents the orientation of the primary direction, and the thin white line represents the orientation of the secondary direction (Figure 17a,18a,20,21). The length of the black line is constant for all stations and the length of the white line varies depending on the number of measurements of ϕ_{sec} with respect to the number of measurements of ϕ_{pri}. The length of the white line represents the ratio between the number of measurements of ϕ_{pri} and ϕ_{sec} thus representing the strength of ϕ_{sec} (Figure 17a,18a,20,21). As shown in Table 5 (localized seismicity SWS results) and Table 6 (regional seismicity results), we gather primary and secondary fast directions for 35 and 62 stations respectively. are mostly perpendicular or quasi-perpendicular to each other with an absolute difference in orientation between 59° and 126°.

Spatial patterns of shear wave splitting from localized seismicity

Based on results from localized seismicity shown in Figure 17. The primary and secondary fast directions are mostly perpendicular or quasi-perpendicular to each other with an absolute difference in orientation between 54° and 126°. At the eight selected stations, ϕ_{pri} and ϕ_{sec} are sub-perpendicular to each other. However, at stations FNO, GORE, OK009, OK020, OK022, and PW17 ϕ_{pri} and ϕ_{sec} are perpendicular to each other. We will discuss the spatial patterns for each of the four regions separately:

In southern Kansas area, the primary fast direction (ϕ_{pri}) of most stations show a NE – SW preferred orientation, whereas the secondary fast directions (ϕ_{sec}) show a preferred NW – SE orientation, denoting obliquity between these two preferred orientations. The polar histograms of the two representative stations (KAN01 and KAN10) clearly show such pattern (Figure 17b). However, station KAN13 that is located near the state boundary, shows significantly gentler ϕ_{pri} orientation in comparison to other stations in the area.

In the Pawnee area, we observe more complex patterns than in Kansas, but the fast directions of polarization can still be grouped spatially, where at the majority of stations ϕ_{pri} shows a preferred ENE – WSW orientation, except station PW11 which shows a preferred NNW – SSE ϕ_{pri} orientation. . ϕ_{sec} do not show a general trend in the area, but ϕ_{pri} and ϕ_{sec} are parallel (PW17) or subparallel to each other. The polar histograms of the representative stations (PW11 and PW14) clearly show such behavior (Figure 17c).

The Fairview area also shows complex patterns with no predominant ϕ_{pri} in the region. However, the relation between ϕ_{pri} and ϕ_{sec} at all stations denotes perpendicular or sub-perpendicular behavior. Figure 17d displays such relationship in the polar histograms of the representative stations (FW03 and OK039). On the other hand, among the stations, there are two

preferred patterns of fast polarization. (1) The representative stations (FW03 and OK039) and stations FW04, FW09, and OK041 show a preferred ϕ_{pri} in the NW-SE orientation, and a ϕ_{sec} in the NE – SW direction, except for station FW09, which shows a prefer ϕ_{sec} in the N – S orientation. (2) Stations FW10, OK035, OK036, and OK042 show a dominant ϕ_{pri} in the NE – SW orientation, and a ϕ_{sec} in the NW – SE direction.

Finally, in central Oklahoma, we observe a general trend of E – W ϕ_{pri} directions and N – S ϕ_{sec} directions at most stations in this region. The representative stations show perpendicular (FNO) and quasi-perpendicular (SMO) behavior between ϕ_{pri} and ϕ_{sec}. The polar histograms of the representative stations show such behavior (Figure 17e). Stations SMO, OK021, OK022, and OK028 show a preferred NE – SW ϕ_{pri} orientation and a preferred NW – SE ϕ_{sec} orientation. Station V35A, shows a peculiar behavior for this region by denoting a preferred ϕ_{pri} in the NW-SE orientation and ϕ_{sec} in the E – W direction, which is opposite to other stations in the region.

Spatial patterns of shear wave splitting from regional seismicity

Based on results from localized seismicity shown in Figure 18. The primary and secondary fast directions are mostly perpendicular or quasi-perpendicular to each other with an absolute difference in orientation between 54° and 144°. At the eight representative stations, ϕ_{pri} and ϕ_{sec} show sub-perpendicular or perpendicular behavior. Stations KAN01, KAN10, and FNO show perpendicular behavior. We will discuss the general spatial patterns for each of the four regions separately and the main differences with localized seismicity results:

In southern Kansas area, in contrast to localized seismicity results (Figure 17a), the primary fast direction (ϕ_{pri}) of most stations show a quasi-north preferred orientation, whereas the secondary fast directions (ϕ_{sec}) show a preferred E-W orientation, denoting orthogonality between these two preferred orientations. The polar histograms of the two representative stations (KAN01

and KAN10) clearly show such pattern (Figure 18b). However, station KAN13 that is located near the state boundary, shows a preferred NE-SW orientation for ϕ_{pri} and a N-S preferred orientation for ϕ_{sec}, in correspondence to the results from localized seismicity.

In the Pawnee area, we observe good correspondence between the localized seismicity results (Figure 17a,c) and the regional seismicity results (Figure 18a,c). However, station PW11 show a ϕ_{pri} in the ENE – WSW direction and a ϕ_{sec} in the NNW – SSE direction, which denotes alternation between fast polarization direction in comparison to the results obtain from localized seismicity.

The Fairview area shows excellent correspondence between localized (Figure 17a,d) and regional seismicity (Figure 18a,d) results. The fast polarization directions show the same preferred orientations as the localized seismicity results, but the regional results show slightly stepper azimuths.

Finally, in central Oklahoma, we observe good correspondence between localized seismicity results (Figure 17a) and regional seismicity results (Figure 18a). There are few exceptions like stations OK028 and station V35A that show alternation between fast polarization directions in comparison to localized seismicity results.

Temporal patterns of shear wave splitting

In contrast to previous studies, like *Nolte et al., (2017)*, where significant fluctuations of fast polarization directions (ϕ) were detected over time in Southern Kansas and Northern Oklahoma. In this study, we did not observe any major time dependent fluctuations of fast polarization directions (ϕ) for our regional seismicity results. On Figure 19, we observe the distribution of the fast polarization directions over time for six stations, one station from each region (KAN01, RH11, OK035 and FNO) and two of the longest recording stations in the central

USA (X37A and WMOK). The data is plotted as 2-D histograms. On the vertical axis, the data is divided into 30 bins, where each bin is 6 degrees long. On the horizontal axis, the data is divided into 20 bins, where each bin is 0.5 years long. On the temporal domain, the bins where normalized to highlight the highest density of fast direction measurements in the vertical axis.

Station KAN01 (Figure 19a), show that the directions of polarization are stable over time, ϕ_{pri} around 0° and ϕ_{sec} around -90° or 270° as displayed on the polar histogram on Figure 18b. There are some minor fluctuations at the beginning on 2019 for ϕ_{pri} and ϕ_{sec}. Station RH11 (Figure 19b), shows that ϕ_{pri} is mostly stable over time around -72° or 288°, it shows minor fluctuations of ± 10° in 2015. On the other hand, ϕ_{sec} is mostly stable around 36°, there are minor fluctuations of ± 5° in 2015. Station OK035 (Figure 19c) shows that ϕ_{pri} and ϕ_{sec} are mostly stable over time around 60° and -30° or 330°respectively. There are some minor fluctuations of ± 5° at the end of 2015 and beginning of 2016 for both directions. Station FNO (Figure 19d) show some minor fluctuations, specially between 2012 and 2014. However, the two fast directions of polarization still are very distinguishable between each other. ϕ_{pri} is mostly stable around 90°, it shows minor fluctuations of ± 5°. ϕ_{sec} is mostly stable around 0°, shows some fluctuations of ± 15°. Station X37A (Figure 19e) shows a ϕ_{pri} with stability over time around 6°, there are some minor fluctuations of ± 15 in 2016 and 2017. On the other hand, ϕ_{sec} is mostly stable around 84° with minor fluctuations of ± 5 in 2012 and 2018. Finally, station WMOK shows that ϕ_{pri} is stable over time around -72° or 288° and ϕ_{sec} is stable around 18°. There are some minor fluctuations of ± 15 in 2010, 2011, and 2018 for both stations.

Discussion

Our localized and regional shear wave splitting results from nine years of data provides a complete SWS parameters dataset for 35 (Table 5) and 62 (Table 6) stations in Oklahoma and Southern Kansas respectively. The relationship between fast polarization directions (ϕ), primary and secondary, and the maximum shear stress orientations (σ_{max}) is shown on Figure 20 for localized results and on Figure 21 for regional results. In both cases, we agree with the observations presented in *Cochran et al., (2020),* where the orientation of ϕ_{pri} corresponds to previously calculated shear stress orientations. In this study, we compare our SWS results with σ_{max} measurements presented by *Qin et al. (2019)* or the World Stress Map (WSM) website (*Heidbach et al., 2016, 2018*). The agreement between ϕ and σ_{max} orientations at the regional level implies that ϕ are extremely sensitive to horizontal stresses and is generally consistent with *Cochran et al., (2020)*.

From localized seismicity observations (Figure 20), in southern Kansas, there is not a clear general correlation between ϕ_{pri} and σ_{max} orientations. At station KAN13 ϕ_{pri} and σ_{max} show a direct correlation and at station KAN10 ϕ_{pri} and σ_{max} are similarly orientated, but there is not a direct correlation. However, there is a good correspondence between ϕ_{sec} and the seismogenic faults in this area (for seismogenic fault orientation refer to *Qin et al., 2019*). On the other hand, from regional seismicity observations (Figure 21), there is a good correlation between ϕ_{sec} and $\sigma_{max.}$ Comparison between statistical analysis of fast directions between localized and regional results (Figure 22), suggests that the primary fast polarization is controlled by horizontal stresses in the area and the secondary fast polarization is controlled by subsurface structures and crustal heterogeneities.

In Pawnee, from both localized (Figure 20) and regional (Figure 21) seismicity results, there is good correlation between ϕ_{pri}, σ_{max}, and seismogenic faults (*Qin et al., 2019*) in the area at multiple stations. From Figure 23, we can suggest that fast polarization directions in this region are mostly influenced by shear stresses in the area. The presence of the ϕ_{sec} is probably caused by local stress perturbations caused by seismogenic faults. In the localized statistical analysis (Figure 23a), we observe more define polarization directions in comparison to regional statistical analysis (Figure 23b). The primary fast polarization directions differ between the localized and regional statistical analyses. This is probably caused by stress perturbation along the ray path of further events considered in the regional statistical analysis. However, the secondary fast polarization directions show a similar orientation in both localized and regional analyses.

In Fairview, most of the stations show perpendicularity between the fault systems in this region and the ϕ_{pri} at these stations. At stations OK036, OK039, and OK041, there is good correspondence between ϕ_{pri}, σ_{max}, seismogenic and sedimentary faults (*Qin et al., 2019*) in this area from localized (Figure 20) and regional (Figure 21) seismicity results. Stations OK035 and FW09 show close resemblance between ϕ_{pri} and σ_{max} (Figure 20 and 21). Comparison between statistical analysis of fast polarization directions between localized and regional results (Figure 24), suggests that shear stress, seismogenic and sedimentary faults are the major controllers of crustal anisotropy in the area.

Central Oklahoma shows the best correlation between ϕ_{pri} and σ_{max}, from both localized (Figure 20) and regional (Figure 21) results. These fast polarization directions (ϕ) are parallel to the fault systems in this area. Stations in the southeast corner of these region are not bounded by fault systems of significant geological structures. From Figure 25, we can suggest that horizontal stresses are the driven factor of fast polarization direction in the area.

Conclusion

We performed a regional shear wave splitting analysis to identify spatial patterns of anisotropy in the central USA over the last nine years (2010 – 2019). We obtained 7,916 high-quality SWS parameters from localized seismicity at 35 stations and 384,325 high-quality splits from regional seismicity at 62 stations in Oklahoma and southern Kansas. We present a shear wave splitting dataset, for both localized and regional seismicity, that is fully reproducible due to the implementation of completely automated methodologies. We observed that in both cases all stations show the presence of a preferred primary fast direction of polarization (ϕ_{pri}) and a secondary fast direction of polarization (ϕ_{sec}). At most stations in Oklahoma, the primary fast direction of polarization (ϕ_{pri}) correlates with the orientation of shear stresses in the region (σ_{max}) obtained from focal mechanism inversions (*Qin et al., 2019*) and world stress map (WSM) measurements (*Heidbach et al., 2016, 2018*). However, some stations show small deviations between ϕ_{pri} and σ_{max} orientations. These discrepancies are potentially caused by local structures in the area (e.g. Fault networks). The secondary fast direction of polarization (ϕ_{sec}) is potentially caused by local stress perturbations in the area. *Cochran et al., (2020)* suggest that such perturbations may indicate the presence of shear fabric aligned sub-parallel to main faults in the region. This shear wave splitting catalog could be a important tool to better understand crustal anisotrphy and its relationship with shear stress orientations (σ_{max}) in the central USA.

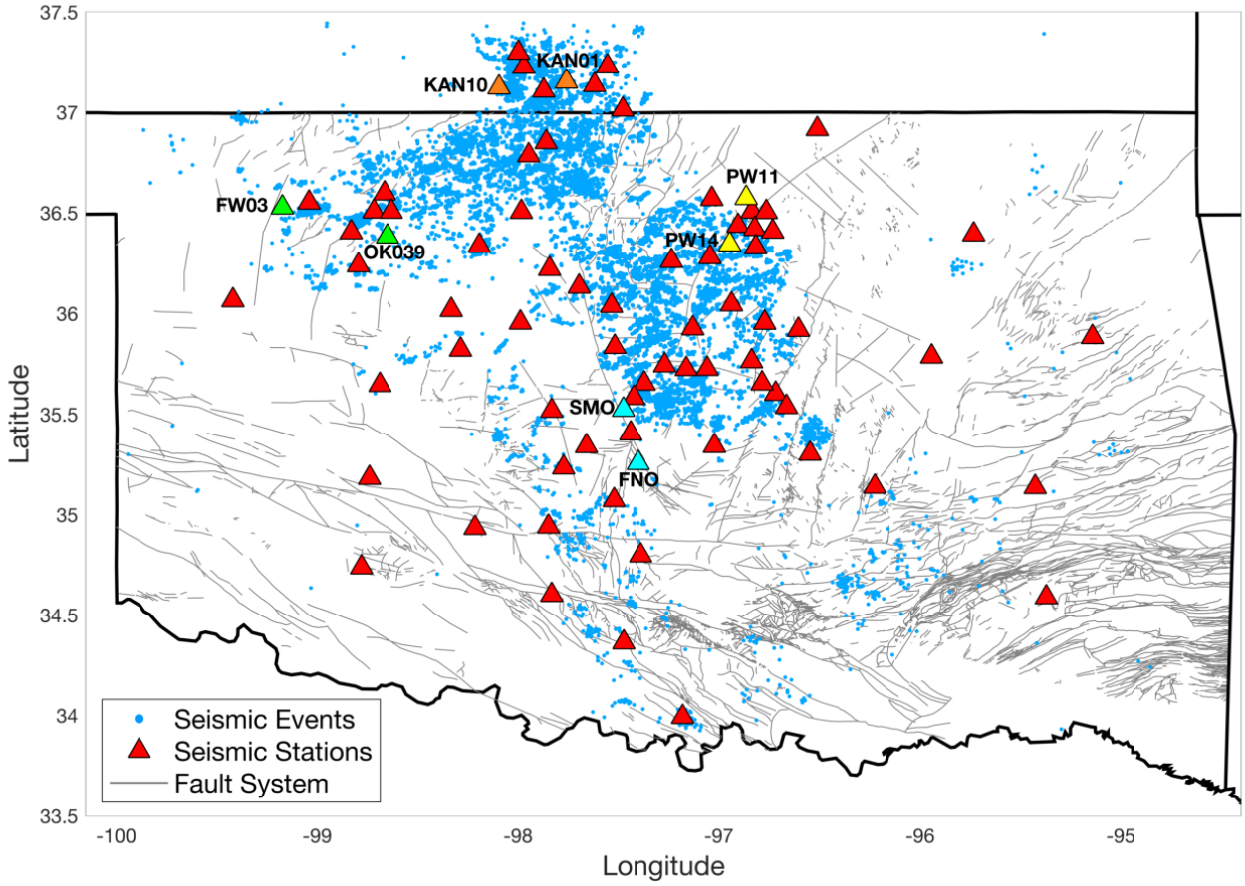

Figure 16. Oklahoma map displaying the seismic sequence distribution (blue dots) between 2010 and 2019, the fault systems (gray lines), and the stations location included in this study (red triangles). The interest areas are as follows: 1. Kansas: stations KAN01 and KAN10 (orange); 2. Fairview: stations FW03 and OK039 (green); 3. Pawnee: stations PW11 and PW14 (yellow); 4. Central Oklahoma: stations FNO and SMO (cyan).

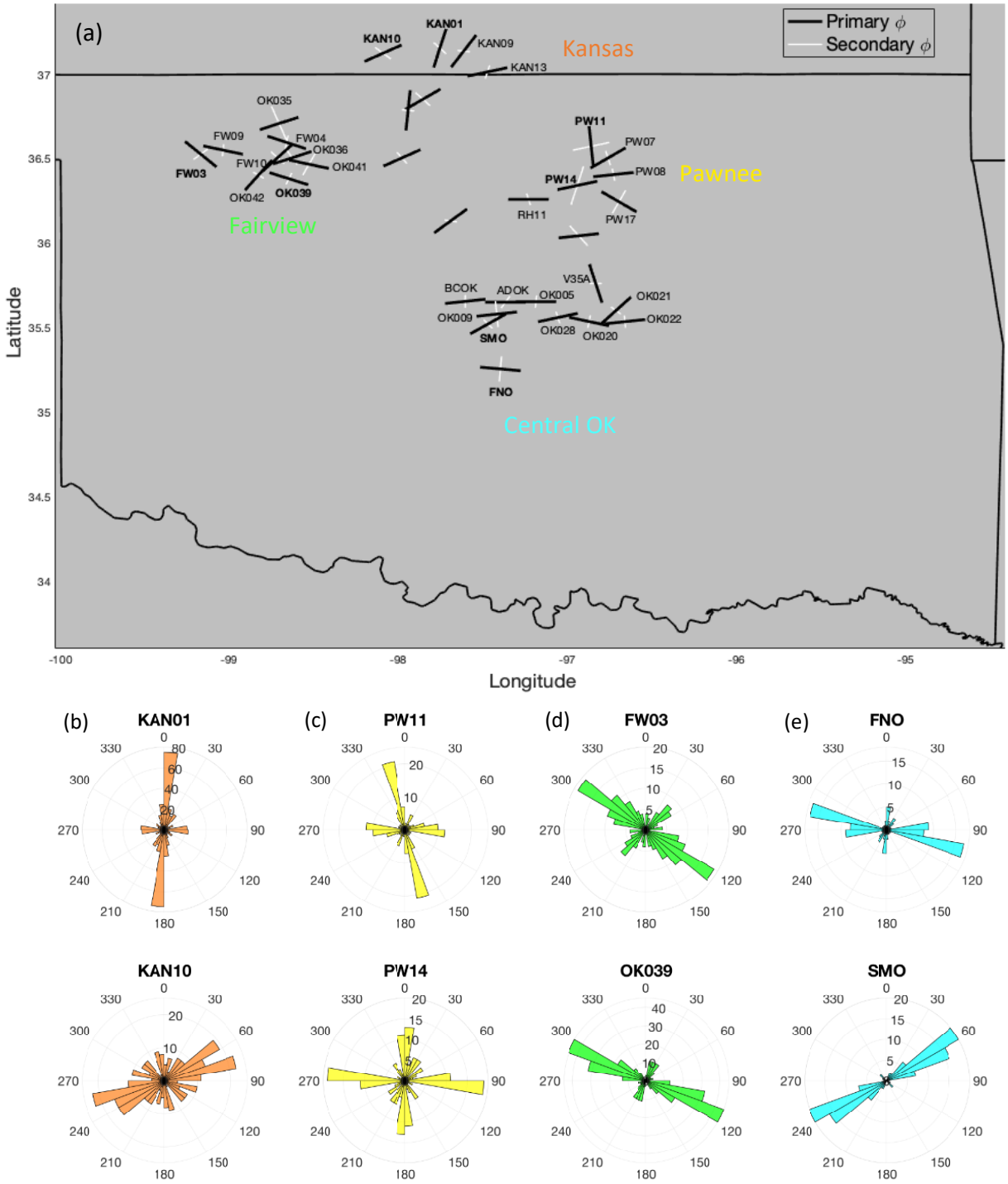

Figure 17. Localized seismicity results. Regional map of Oklahoma and southern Kansas seismic network showing primary (black) and secondary (white) ϕ directions at each station. Polar histograms for the six isolated stations. Kansas (orange): KAN01 (ϕ_{pri}:18° – ϕ_{sec}: 48°) and KAN10 (ϕ_{pri}:66° – ϕ_{sec}: -54°). Fairview (green): FW03 (ϕ_{pri}: -54° – ϕ_{sec}: 60°) and OK039 (ϕ_{pri}: -73° – ϕ_{sec}: 36°). Pawnee (yellow): PW11 (ϕ_{pri}: 6° – ϕ_{sec}: 78°) and PW14 (ϕ_{pri}: 78° – ϕ_{sec}: 18°). Central Oklahoma (cyan): FNO (ϕ_{pri}: 95° – ϕ_{sec}: 5°) and SMO (ϕ_{pri}: 61° – ϕ_{sec}: -46°).

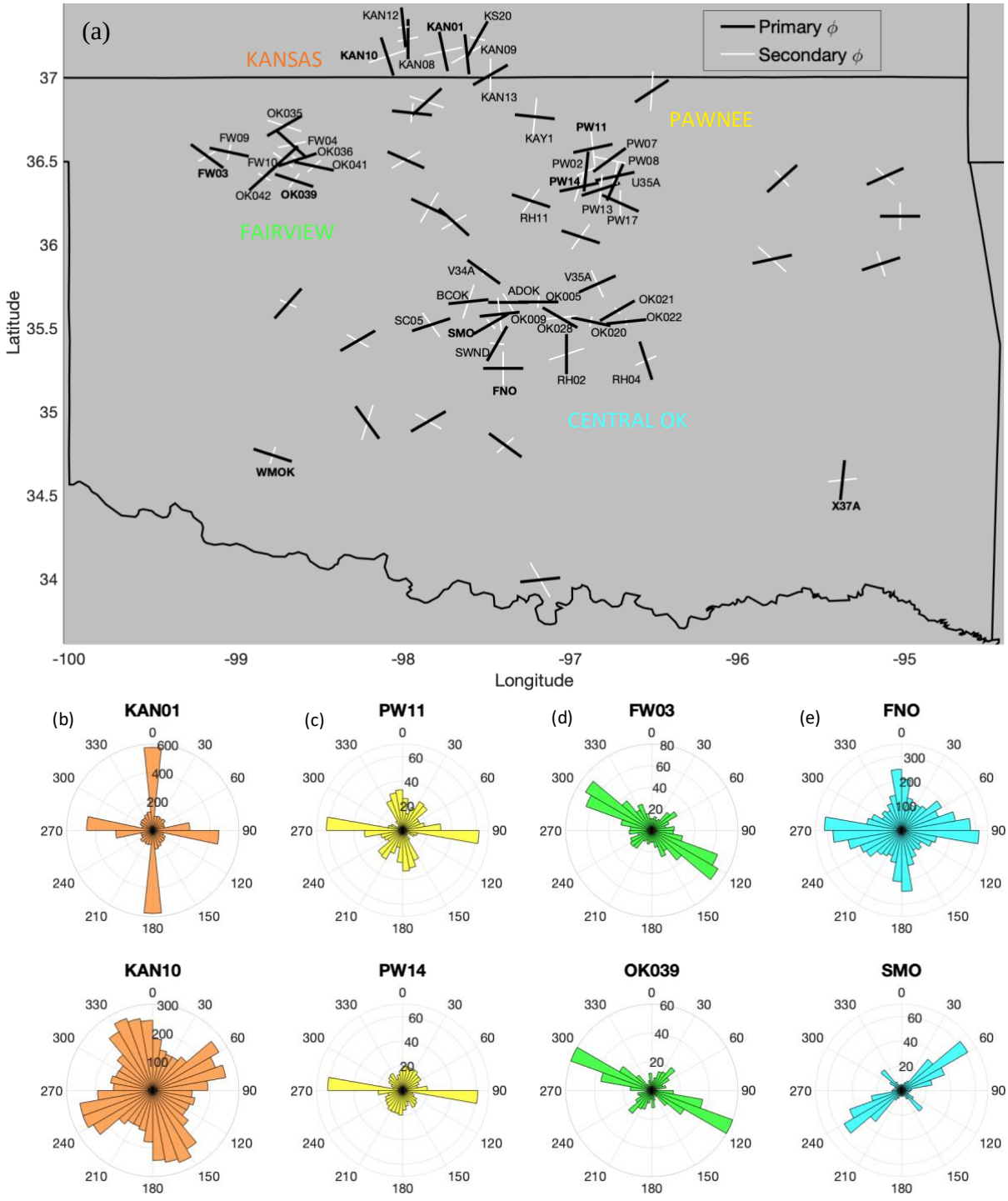

Figure 18. Regional seismicity results. Regional map of Oklahoma and southern Kansas seismic network showing primary (black) and secondary (white) ϕ directions at each station. Polar histograms for the six isolated stations. Kansas (orange): KAN01 (ϕ_{pri}: -12° – ϕ_{sec}: 78°) and KAN10 (ϕ_{pri}: -18° – ϕ_{sec}: 72°). Fairview (green): FW03 (ϕ_{pri}: -51° – ϕ_{sec}: 53°) and OK039 (ϕ_{pri}: -72° – ϕ_{sec}: 36°). Pawnee (yellow): PW11 (ϕ_{pri}: 78° – ϕ_{sec}: -6°) and PW14 (ϕ_{pri}: 78° – ϕ_{sec}: 18°). Central Oklahoma (cyan): FNO (ϕ_{pri}: 90° – ϕ_{sec}: 0°) and SMO (ϕ_{pri}: 60° – ϕ_{sec}: -42°).

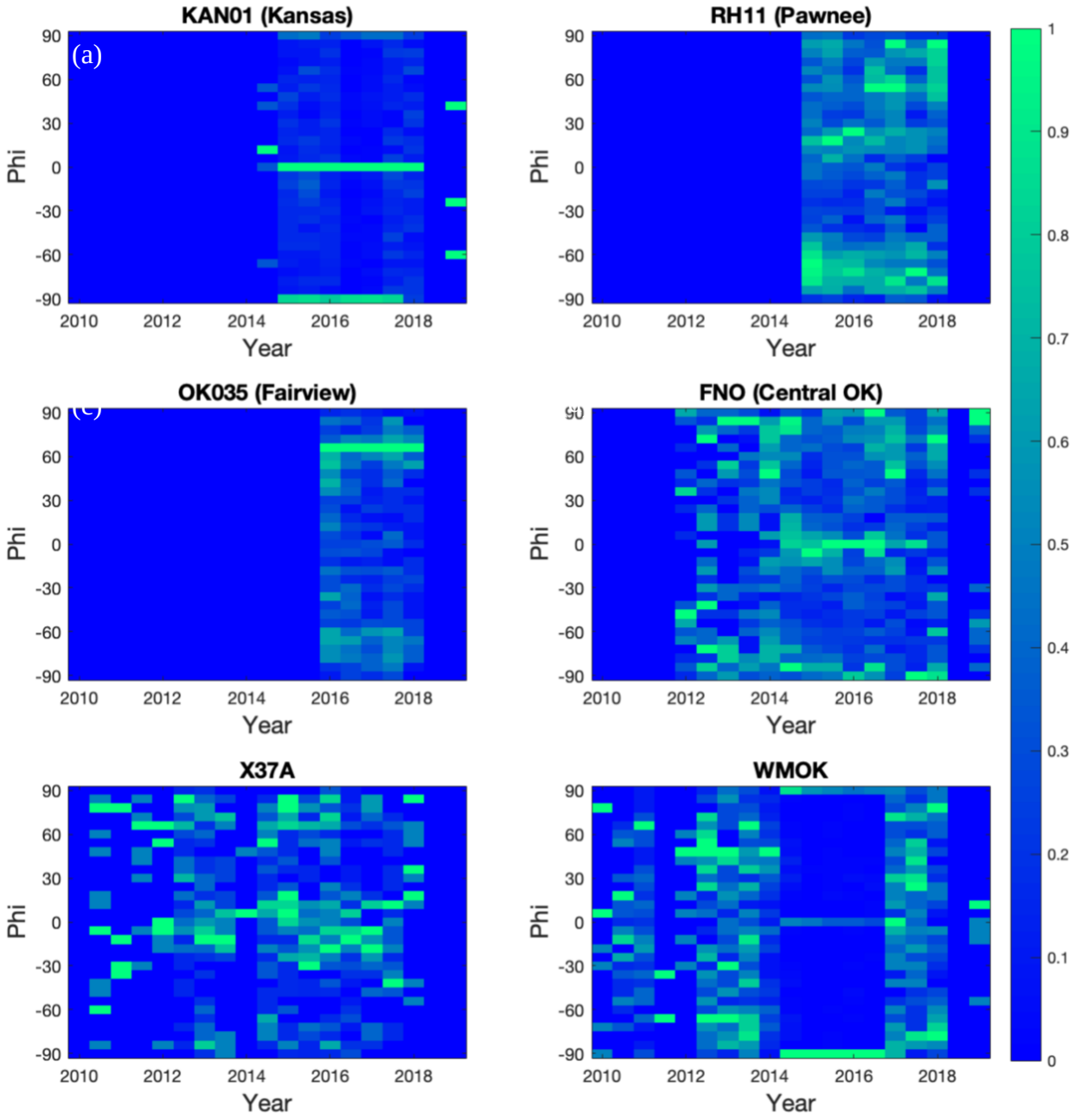

Figure 19. Fast polarization directions over time. 2D histograms for four of the isolated stations: KAN01, RH11, OK035, FNO, X37A, and WMOK. On the vertical axis, the data is divided into 30 bins, where each bin is 6 degrees long. On the horizontal axis, the data is divided into 20 number of bins, where each bin is 0.5 years long.

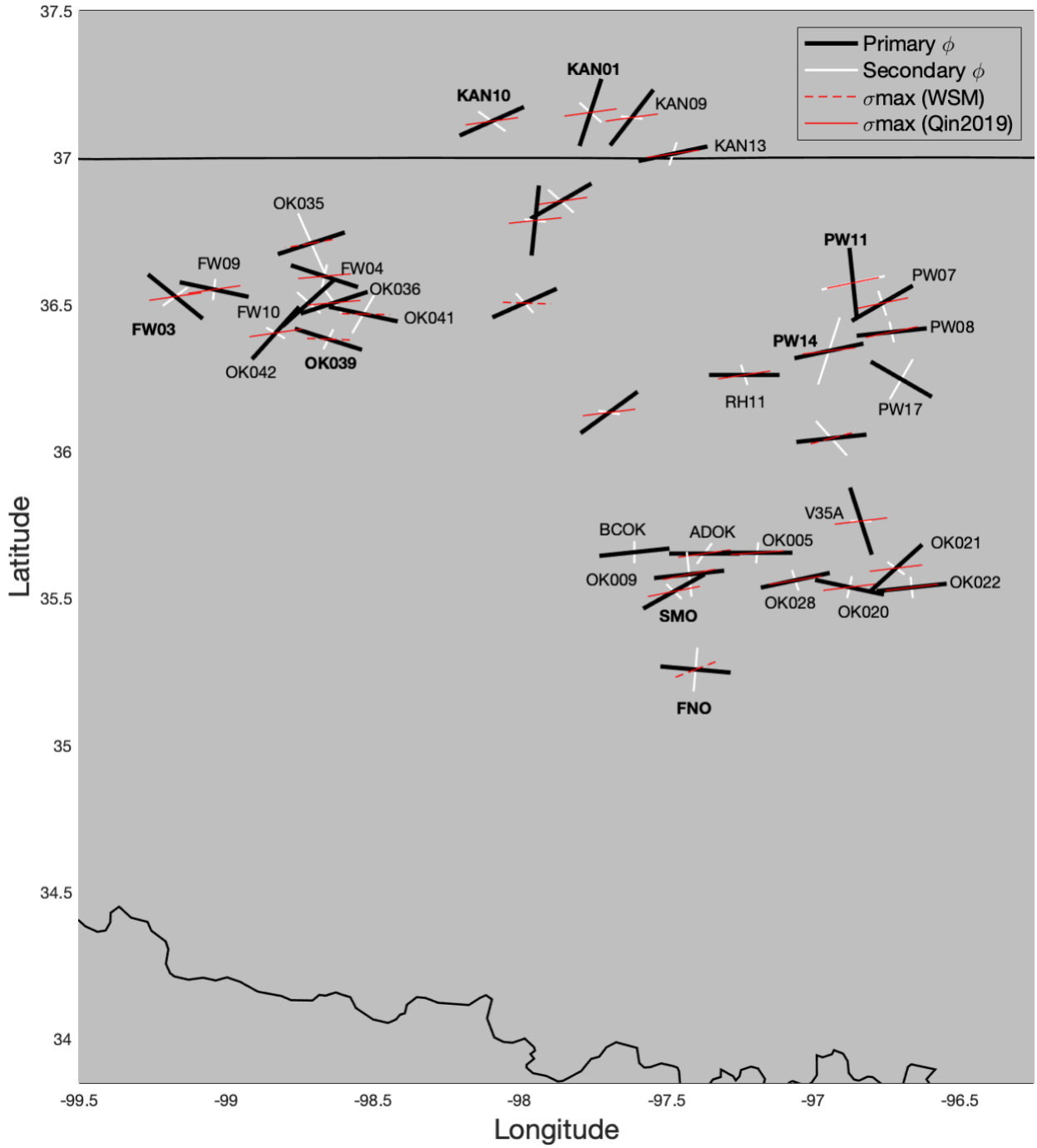

Figure 20. Regional comparison between primary (black) and secondary (white) ϕ directions from localized seismicity and σmax orientations. Red dashed line: world stress map (wsm) measurements. Red solid line: *Qin et al., (2019)* measurements.

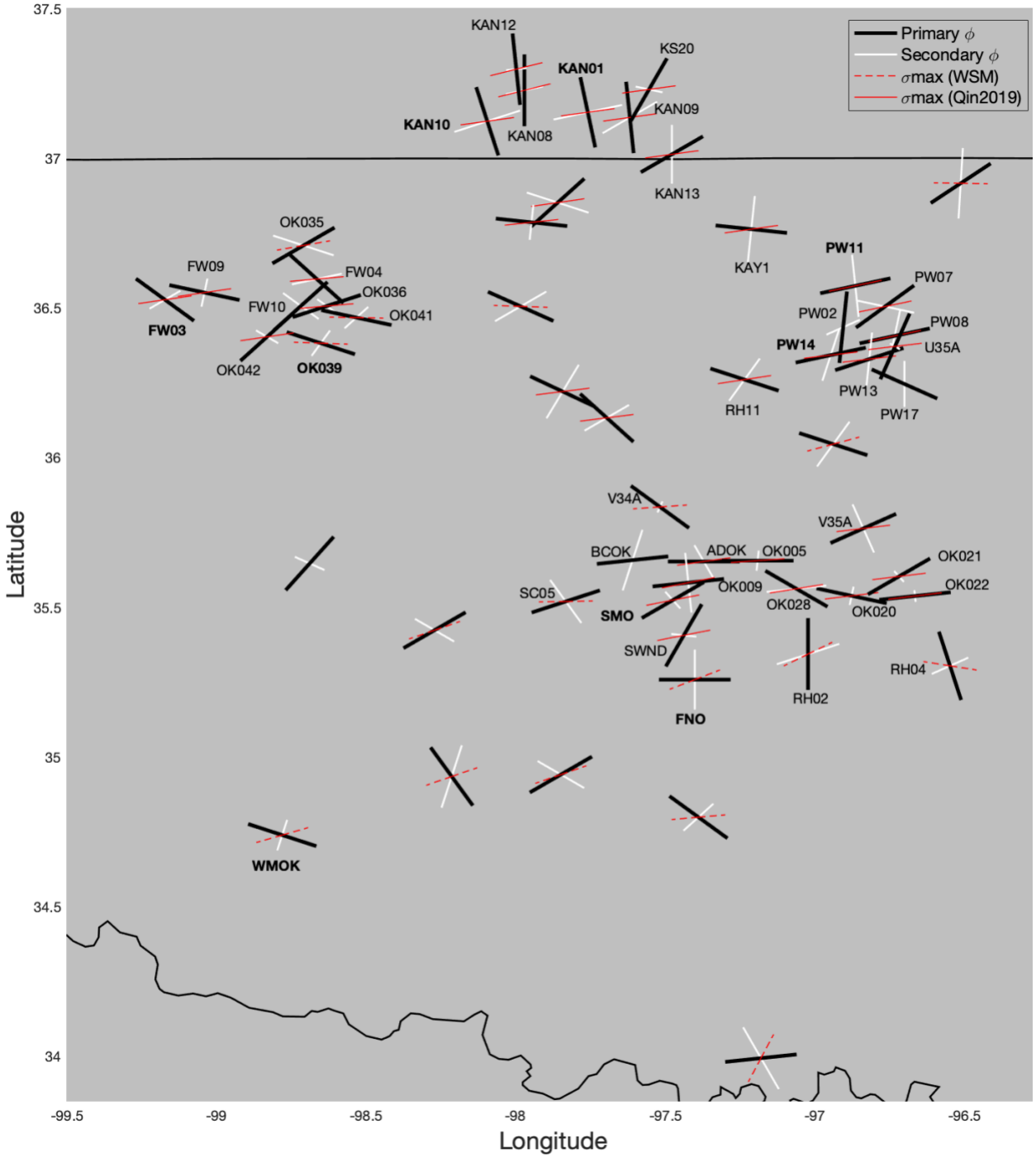

Figure 21. Regional comparison between primary (black) and secondary (white) ϕ directions from regional seismicity and *σ*max orientations. Red dashed line: world stress map (wsm) measurements. Red solid line: *Qin et al., (2019)* measurements.

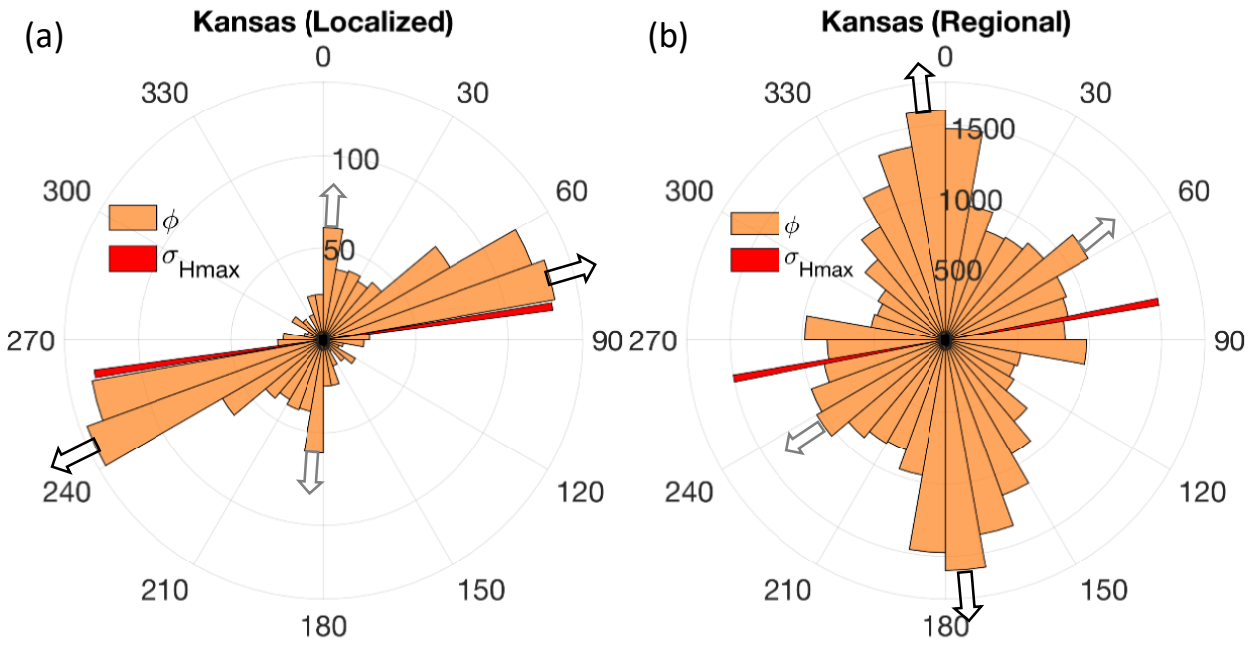

Figure 22. Statistical analysis of fast polarization directions (ϕ) in southern Kansas and comparison with average regional σmax orientations (*Qin et al., 2019*). (a) Localized seismicity. (b) Regional seismicity.

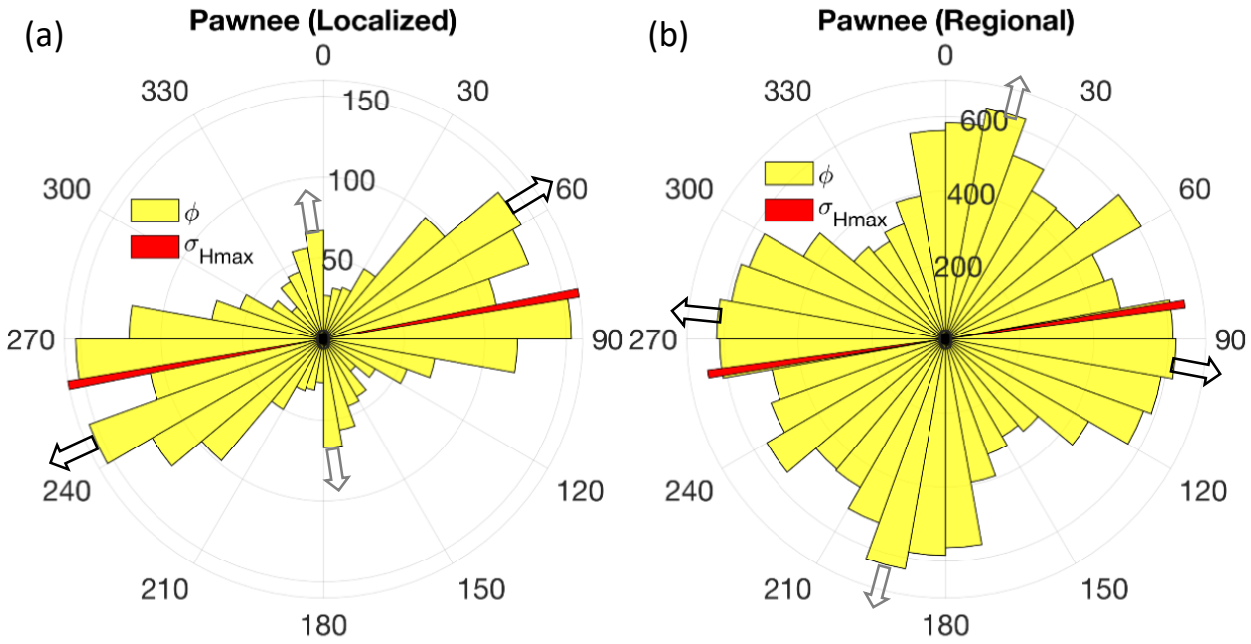

Figure 23. Statistical analysis of fast polarization directions (ϕ) in Pawnee and comparison with average regional σmax orientations (*Qin et al., 2019*). (a) Localized seismicity. (b) Regional seismicity.

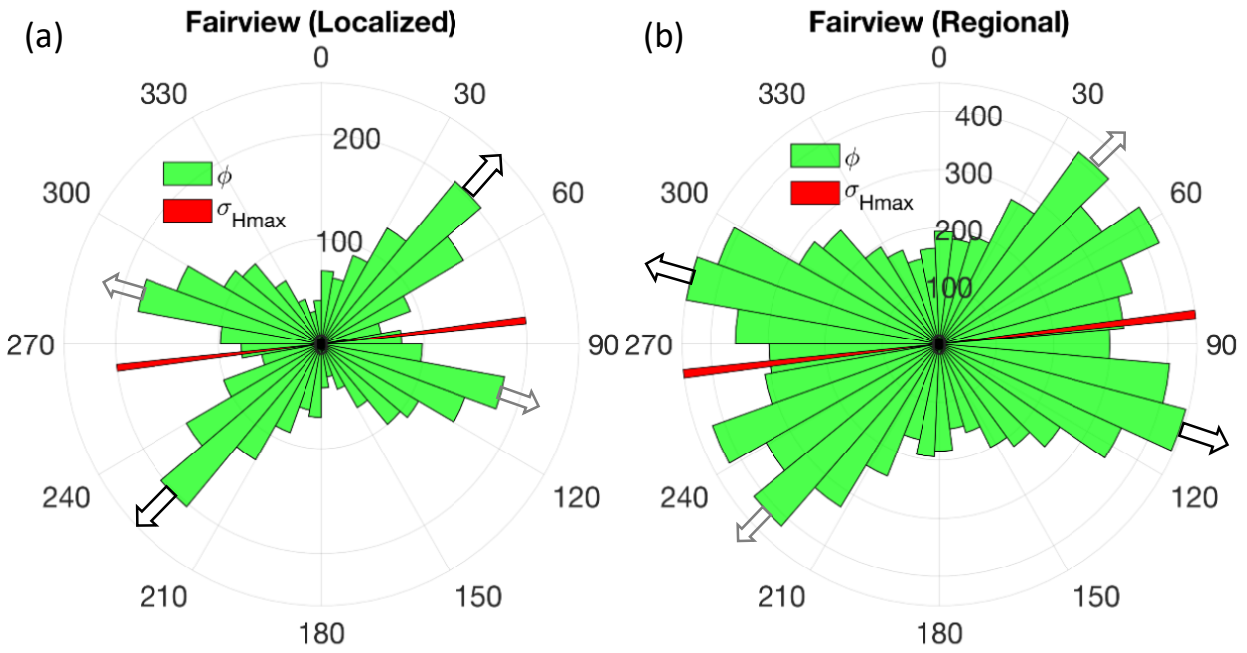

Figure 24. Statistical analysis of fast polarization directions (ϕ) in Fairview and comparison with average regional σmax orientations (*Qin et al., 2019*). (a) Localized seismicity. (b) Regional seismicity.

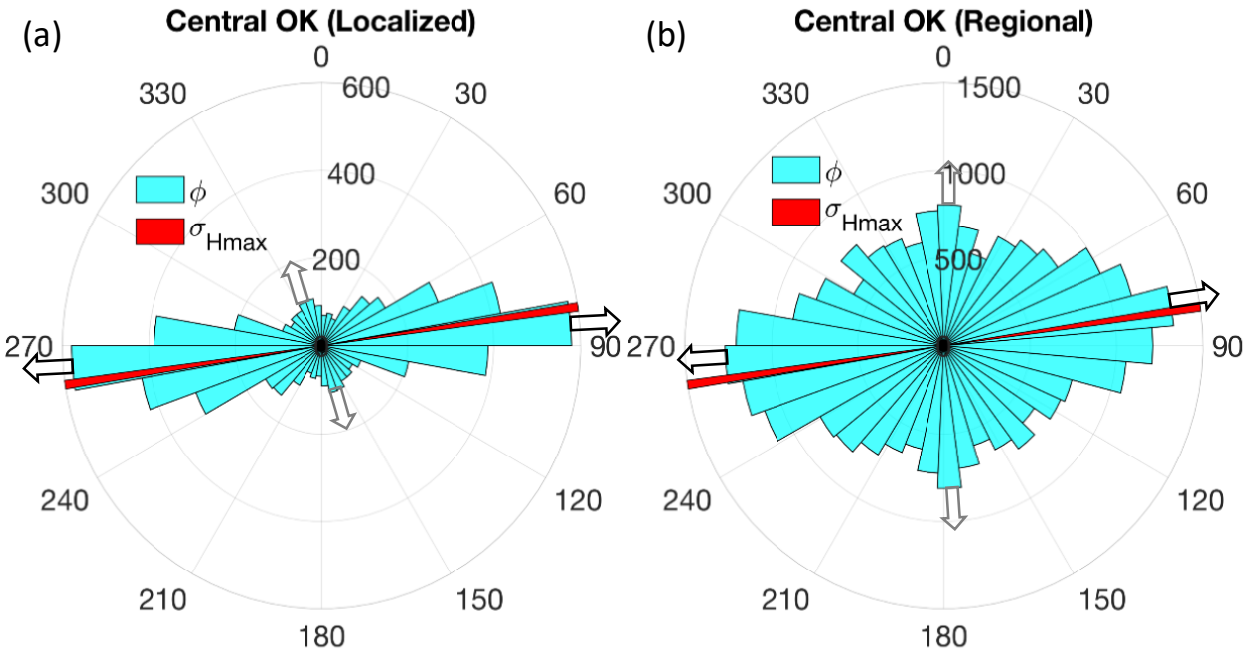

Figure 25. Statistical analysis of fast polarization directions (ϕ) in central Oklahoma and comparison with average regional σmax orientations (*Qin et al., 2019*). (a) Localized seismicity. (b) Regional seismicity.

#	Station	Region	ϕ_{PRI}†	ϕ_{SEC}‡	σ_{max}¶	Abs. Diff. $\lvert\phi_{pri} - \phi_{sec}\rvert$§	Abs. Diff. $\lvert\phi_{pri} - \sigma_{max}\rvert_{\|}$
1	ADOK	Central OK	90	36	82	54	8
2	BCOK	Central OK	84	0	79	84	5
3	CROK	N/A	66	-42	92*	108	26
4	FNO	Central OK	95	5	69*	90	26
5	FW03	Fairview	-51	53	82	104	47
6	FW04	Fairview	72	12	85	60	13
7	FW09	Fairview	78	6	82	72	4
8	FW10	Fairview	48	-48	85	96	37
9	GC02	N/A	60	-48	82	108	22
10	GORE	N/A	6	96	84	90	78
11	KAN01	Kansas	18	-48	82	66	64
12	KAN09	Kansas	38	96	82	58	44
13	KAN10	Kansas	66	-54	76	120	10
14	KAN13	Kansas	78	18	82	60	4
15	KNG1	N/A	54	99	83	45	29
16	OK005	Central OK	90	6	86	84	4
17	OK009	Central OK	84	-6	79	90	5
18	OK020	Central OK	102	12	83	90	19
19	OK021	Central OK	48	-54	83	102	35
20	OK022	Central OK	84	-6	83	90	1
21	OK028	Central OK	78	-18	81	96	3
22	OK033	N/A	84	-42	75*	126	11
23	OK035	Fairview	72	-24	80*	96	8
24	OK036	Fairview	72	-36	85	108	13
25	OK039	Fairview	73	26	85	46	12
26	OK041	Fairview	102	30	91*	72	11
27	OK042	Fairview	42	-60	82	102	40
28	PW07	Pawnee	60	-18	78	78	18
29	PW08	Pawnee	84	-12	78	96	12
30	PW11	Pawnee	6	78	78	72	72
31	PW14	Pawnee	78	18	83	60	5
32	PW17	Pawnee	-60	30	83	90	37
33	RH11	Pawnee	90	-18	81	108	11
34	SMO	Central OK	61	-46	79	107	18
35	V35A	Central OK	18	90	83	72	65

Table 5. Shear wave splitting parameters database for Oklahoma and southern Kansas from localized seismicity at 35 seismic stations. †Primary fast direction of polarization. ‡Secondary fast direction of polarization. ¶Maximum shear stress orientations (*Qin et al., 2019)*. *Maximum shear stress orientations (wsm). §Absolute difference between primary and secondary fast

directions of polarization. ‖Absolute difference between primary fast direction of polarization and maximum shear stress orientations. All measurements are presented in degrees from north.

#	Station	Region	ϕ_{PRI}†	ϕ_{SEC}‡	σ_{max}¶	Abs. Diff. $\lvert\phi_{pri} - \phi_{sec}\rvert$§	Abs. Diff. $\lvert\phi_{pri} - \sigma_{max}\rvert$‖
1	ADOK	Central OK	90	-30	82	120	8
2	BCOK	Central OK	84	18	79	66	5
3	CROK	N/A	-66	60	92*	126	12
4	CSTR	N/A	42	-66	N/A	108	N/A
5	FNO	Central OK	90	0	69*	90	21
6	FW03	Fairview	-54	60	82	114	44
7	FW04	Fairview	-48	78	85	126	47
8	FW09	Fairview	-78	12	82	90	20
9	FW10	Fairview	48	-54	85	102	37
10	GC02	N/A	48	-72	82	120	-34
11	GORE	N/A	96	6	84	90	8
12	KAN01	Kansas	-12	78	82	90	86
13	KAN08	Kansas	0	78	76	78	76
14	KAN09	Kansas	-6	60	82	66	88
15	KAN10	Kansas	-18	72	76	90	86
16	KAN12	Kansas	-6	84	76	90	82
17	KAN13	Kansas	60	0	82	60	22
18	KAY1	Pawnee	96	6	82	90	14
19	KNG1	N/A	-48	60	83	108	49
20	KS20	Kansas	30	-78	82	108	52
21	LOOK	N/A	84	-30	28*	114	56
22	OK005	Central OK	90	6	86	84	4
23	OK009	Central OK	84	-6	79	90	5
24	OK020	Central OK	102	12	83	90	19
25	OK021	Central OK	60	-42	83	102	23
26	OK022	Central OK	84	-6	83	90	1
27	OK028	Central OK	-60	84	81	144	39
28	OK033	N/A	-72	36	75*	108	33
29	OK035	Fairview	60	-30	80*	132	20
30	OK036	Fairview	72	-54	85	126	13
31	OK039	Fairview	-72	36	85	108	23
32	OK041	Fairview	-78	48	91*	126	24
33	OK042	Fairview	48	-60	82	108	34
34	PW02	Pawnee	6	66	78	60	72
35	PW07	Pawnee	54	-78	78	132	24

36	PW08	Pawnee	78	12	78	66	0
37	PW11	Pawnee	78	-6	78	84	0
38	PW13	Pawnee	72	6	83	66	11
39	PW14	Pawnee	78	18	83	60	5
40	PW17	Pawnee	-66	0	83	66	31
41	RH02	Central OK	0	72	64*	72	64
42	RH04	Central OK	-18	66	99*	84	63
43	RH11	Pawnee	-72	36	81	108	27
44	RLOK	N/A	90	0	N/A	90	N/A
45	SC02	N/A	-54	48	85*	102	41
46	SC03	N/A	60	-60	71*	120	11
47	SC05	Central OK	72	-36	89*	108	17
48	SC07	N/A	-36	18	71*	54	73
49	SC10	N/A	60	-60	71*	120	11
50	SC19	N/A	-65	31	83	96	32
51	SMO	Central OK	60	-42	79	102	19
52	SWND	Central OK	30	96	79	66	49
53	T35A	N/A	57	3	91*	54	34
54	TUL3	N/A	78	-48	N/A	126	N/A
55	U35A	Pawnee	24	-60	83	84	59
56	U36A	N/A	48	-42	N/A	90	N/A
57	U37A	N/A	66	-48	N/A	114	N/A
58	V34A	Central OK	-54	24	86*	78	40
59	V35A	Central OK	66	-24	83	90	17
60	V37A	N/A	72	-18	N/A	90	N/A
61	WMOK	N/A	108	18	74*	90	34
62	X37A	N/A	6	84	N/A	78	N/A

Table 6. Shear wave splitting parameters database for Oklahoma and southern Kansas from regional seismicity at 62 seismic stations. †Primary fast direction of polarization. ‡Secondary fast direction of polarization. ¶Maximum shear stress orientations *(Qin et al., 2019)*. *Maximum shear stress orientations (wsm). §Absolute difference between primary and secondary fast directions of polarization. ‖Absolute difference between primary fast direction of polarization and maximum shear stress orientations. All measurements are presented in degrees from north.

Chapter 5: Conclusion

I investigate two of the most seismically active regions in the USA (Hawaii and central USA) by conducting three independent research studies to better understand earthquake clustering behavior and characteristics, subsurface structures, stress orientations, and spatial anisotropy patterns.

In the first study, after concurrently analyzing the volcanic, seismic, and collapsing activities at the summit of Kilauea volcano, I perform a spatiotemporal clustering analysis, following the nearest neighbor approach (*Cheng and Chen, 2018*), on the high-resolution earthquake catalog presented by *Shelly and Thelen (2019)*. I identify two modes (M1 and M2) of naturally occurring clusters. After further analysis of M1(shorter space distance), I find:

- 1,157 clusters of which 45 clusters have 20 or more events, 10 clusters have 10 or more events, and about 500 clusters have at least 2 events.
- The clusters are found as isolated patches of seismicity off the main crater.
- M1 clusters do not show a clear temporal correlation with collapsing events (M5.2 – M5.4).
- M1 clustering behavior correlates with collapsing activity behavior.

I then further analyzed M2 (longer space distance) clustering behavior and find:

- 166 clusters of which 55 clusters have 20 or more events.
- Most of catalog events fall within clusters with more than 20 events.
- 42 clusters with 20 or more events can be classify as a seismicity cycle.
- M2 clusters duration gradually increase over time, from 0.5 to 1.5 days.
- M2 clustering behavior directly correlates to volcanic activity at Kilauea volcano, especially to summit deformation.

Based on M1 and M2 clustering observations, I determinate that the previously classified seismicity cycles are characterized by a period of latent seismicity, followed by a period of significant seismicity increase and finalizing with a Mw5.2 – Mw5.4 caldera collapse. During the entire seismic sequence, there is correlation between earthquake rate and deformation rate. Positive correlation suggests that much of the deformation is accommodated by boundary faults activated during the eruption, and negative correlation suggest that most of the deformation is aseismic likely due to volcano inflation/deflation.

In the second study, I systematically used a technique combining cross-correlation and earthquake crustal reverberation observations to better understand waveform behavior and characteristics for groups of events confined within narrow depth ranges in the Cushing fault zone in Oklahoma. From crustal reverberation analyses I find:

- Crustal reverberations at nine stations on the vertical channel.
- Crustal reverberations at five stations on individual horizontal channels.
- Two to three earthquake clusters with different source depths recorded at individual stations.
- One to three crustal reverberations after the direct wave arrivals at each cluster.
- The relative timing between crustal reverberations is consistent for clusters at different depths.
- The relative amplitude between crustal reverberations varies with source depth, where shallower depth clusters show stronger reverberation arrivals than intermediate and deeper depth clusters.
- Nearly constant delay time for crustal reverberations across wide distance ranges for P and S waveforms.

Based on the consistency of these observations, I conclude that this technique is transferable to nearby regions in Oklahoma and the central USA. This technique plus the implementation of forward modeling can be used to constrain shallow structures depths and earthquake depths relative to the basement interface.

In the third and last study, I performed a regional shear wave splitting analysis in Oklahoma and southern Kansas to analyze spatial patterns of crustal anisotropy in the region. I used the automated technique (MFAST) to obtain shear wave splitting parameters for localized seismicity and regional seismicity from the last nine years (2010 – 2019) of seismicity in the central USA and find:

- We obtained 7,9186 high-quality splits from localized seismicity at 35 seismic stations in Oklahoma and southern Kansas.
- We obtained 384,325 high-quality splits at 62 stations from regional seismicity in Oklahoma and southern Kansas.
- We observed that all stations show the presence of a ϕ_{pri} and ϕ_{sec}.
- ϕ_{sec} are potentially caused by local stress perturbations in the area, local structures or the presence of shear fabric alignments in the region *(Cochran et al., 2020)*.
- In Oklahoma, at most stations, ϕ_{pri} correlates with σ_{max} orientations in the region.
- The small deviations between ϕ_{pri} and σ_{max} orientations are potentially caused by local structures in the area (e.g. Fault networks).
- Localized seismicity results shows a better correlation with σ_{max} orientations.

Based on these observations, I present a shear wave splitting dataset that is fully reproducible due to the implementation of completely automated methodologies. This shear wave splitting catalog

could be considered an important tool to better understand crustal anisotrophy and its relationship with shear stress orientations (σ_{max}) in the central USA.

References

Adams, D. C., & Keller, G. R. (1996). Precambrian basement geology of the Permian basin region of west Texas and eastern New Mexico: A geophysical perspective. *AAPG Bulletin*, *80*(3), 410–431. https://doi.org/10.1306/64ED87FA-1724-11D7-8645000102C1865D

Anderson, K. R., Johanson, I. A., Patrick, M. R., Gu, M., Segall, P., Poland, M. P., Montgomery-Brown, E. K., & Miklius, A. (2019). Magma reservoir failure and the onset of caldera collapse at Kīlauea Volcano in 2018. *Science*, *366*(6470). https://doi.org/10.1126/science.aaz1822

Baird, A. F., Kendall, J. M., Verdon, J. P., Wuestefeld, A., Noble, T. E., Li, Y., Dutko, M., & Fisher, Q. J. (2013). Monitoring increases in fracture connectivity during hydraulic stimulations from temporal variations in shear wave splitting polarization. *Geophysical Journal International*, *195*(2), 1120–1131. https://doi.org/10.1093/gji/ggt274

Butler, R. (2019). Composite earthquake source mechanism for 2018 M w 5.2-5.4 swarm at kīlauea caldera: Antipodal source constraint. *Seismological Research Letters*, *90*(2 A), 633–641. https://doi.org/10.1785/0220180288

Castellazzi, C., Savage, M. K., Walsh, E., & Arnold, R. (2015). Shear wave automatic picking and splitting measurements at Ruapehu volcano, New Zealand. *Journal of Geophysical Research: Solid Earth*, *120*, 3363–3384. https://doi.org/10.1002/2014JB011585.

Chen, X., Haffener, J., Goebel, T. H. W., Meng, X., Peng, Z., & Chang, J. C. (2018). Temporal correlation between seismic moment and injection volume for an induced earthquake sequence in central Oklahoma. *Journal of Geophysical Research: Solid Earth*, (2016), 1–18. https://doi.org/10.1002/2017JB014694

Chen, Chen. (2016). Comprehensive Analysis of Oklahoma Earthquakes: From Earthquake Monitoring to 3D Tomography and Relocation (Doctoral dissertation). https://shareok.org/handle/11244/45025

Cheng, Y., & Chen, X. (2018). Characteristics of seismicity inside and outside the salton sea geothermal field. *Bulletin of the Seismological Society of America*, *108*(4), 1877–1888. https://doi.org/10.1785/0120170311

Cochran, E. S., Skoumal, R. J., McPhillips, D., Ross, Z. E., & Keranen, K. M. (2020). Activation of optimally- and unfavorably-oriented faults in a uniform local stress field during the 2011 Prague, Oklahoma, sequence. *Geophysical Journal International*. https://doi.org/10.1093/gji/ggaa153

Crampin, S. (1984). Effective anisotropic elastic constants for wave propagation through cracked solids. *Geophysical Journal of the Royal Astronomical Society*, *76*(1), 135–145. https://doi.org/10.1111/j.1365-246X.1984.tb05029.x

Denison, R. E., Lidiak, E. G., Bicford, M. E., & Kisvarsanyi, E. B. (1984). Geology and Geochronology of Precambrian Rocks in the Central Interior Region of the United States. *U.S. Geological Survey Professional Paper*, *1241–C*, 1–13.

Darold, A. P., Holland, A. A., Jennifer, K., & Gibson, A. R. (2015). Oklahoma Earthquake Summary Report 2014. *Oklahoma Geological Survey Open File Report*, *OF1-2015*.

Ellsworth, W. L. (2013). Disposal of hydrofracking waste fluid by injection into subsurface aquifers triggers earthquake swarm in central arkansas with potential for damaging earthquake. *Science Advances*, *341*(6142). https://doi.org/10.1126/science.1225942

Frohlich, C., Ellsworth, W. L., Brown, W. A., Brunt, M., Luetgert, J., MacDonald, T., & Walter, S. (2014). The 17 May 2012 M4.8 earthquake near Timpson, East Texas: An event possibly triggered by fluid injection. *Journal of Geophysical Research: Solid Earth*, *119*(June 1981), 581–593. https://doi.org/10.1002/2013JB010755.Received

Fukao, Y. (1984). Evidence from core-reflected shear waves for anisotropy in the Earth's mantle. *Nature*, *309*(5970), 695–698. https://doi.org/10.1038/309695a0

Gao, Y., Wu, J., Fukao, Y., Shi, Y., & Zhu, A. (2011). Shear wave splitting in the crust in North China: Stress, faults and tectonic implications. *Geophysical Journal International*, *187*(2), 642–654. https://doi.org/10.1111/j.1365-246X.2011.05200.x

Heidbach, O., Rajabi, M., Cui, X., Fuchs, K., Müller, B., Reinecker, J., Reiter, K., Tingay, M., Wenzel, F., Xie, F., Ziegler, M. O., Zoback, M. Lou, & Zoback, M. (2018). The World Stress Map database release 2016: Crustal stress pattern across scales. In *Tectonophysics*. https://doi.org/10.1016/j.tecto.2018.07.007

Heidbach, O., Rajabi, M., Reiter, K., Ziegler, M., & Team, W. S. M. (2016). World Stress Map Database Release 2016. In *GFZ Data Services*. https://doi.org/10.5880/WSM.2016.001

Hill, D. P. (1974). Phase shift and pulse distortion in body waves due to internal caustics. *Bulletin Of The Seismological Society Of America*.

Johnson, J. H., & Savage, M. K. (2012). Tracking volcanic and geothermal activity in the Tongariro Volcanic Centre, New Zealand, with shear wave splitting tomography. *Journal of Volcanology and Geothermal Research*, *223–224*, 1–10. https://doi.org/10.1016/j.jvolgeores.2012.01.017

Keller, G. R., & Stephenson, R. A. (2007). The Southern Oklahoma and Dniepr-Donets aulacogens: A comparative analysis. *GSA Memoir*, *200*, 127–143. https://doi.org/10.1130/2007.1200(08)

Keranen, K. M., Weingarten, M., Abers, G. A., Bekins, B. A., & Ge, S. (2014). Sharp increase in central Oklahoma seismicity since 2008 induced by massive wastewater injection. *Science*. https://doi.org/10.1126/science.1255802

Langston, C. a. (2003). Local Earthquake Wave Propagation through Mississippi Embayment Sediments, Part I: Body-Wave Phases and Local Site Responses. *Bulletin of the Seismological Society of America*, *93*(6), 2664–2684. https://doi.org/10.1785/0120030046

Li, Z., & Peng, Z. (2016). An Automatic Phase Picker for Local Earthquakes with Predetermined Locations: Combining a Signal-to-Noise Ratio Detector with 1D Velocity Model Inversion. *Seismol. Res. Lett.*, *87*(6). https://doi.org/10.1785/0220160027

Li, Z., & Peng, Z. (2017). Stress- and Structure-Induced Anisotropy in Southern California From Two Decades of Shear Wave Splitting Measurements. *Geophysical Research Letters*, *44*(19), 9607–9614. https://doi.org/10.1002/2017GL075163

McGarr, A. (2014). Maximum magnitude earthquakes induced by fluid injection. *Journal of Geophysical Research: Solid Earth*. https://doi.org/10.1002/2013JB010597

McGarr, A., & Barbour, A. J. (2017). Wastewater Disposal and the Earthquake Sequences During 2016 Near Fairview, Pawnee, and Cushing, Oklahoma. *Geophysical Research Letters*. https://doi.org/10.1002/2017GL075258

McNamara, D. E., Hayes, G. P., Benz, H. M., Williams, R. A., McMahon, N. D., Aster, R. C., Holland, A., Sickbert, T., Herrmann, R., Briggs, R., Smoczyk, G., Bergman, E., & Earle, P. (2015). Reactivated faulting near Cushing, Oklahoma: Increased potential for a triggered earthquake in an area of United States strategic infrastructure. *Geophysical Research Letters*. https://doi.org/10.1002/2015GL064669

Mori, J. (1991). Estimates of velocity structure and source depth using multiple P waves from aftershocks of the 1987 Elmore Ranch and Superstition Hills, California, earthquakes. *Bulletin of the Seismological Society of America*, *79*(2), 508–523. Retrieved from http://www.bssaonline.org/cgi/content/abstract/81/2/508

Neal, C. A., Brantley, S. R., Antolik, L., Babb, J. L., & Etc. (2019). The 2018 rift eruption and summit collapse of Kīlauea Volcano. *Science*, *363*(January), 367–374.

Nolte, K. A., Tsoflias, G. P., Bidgoli, T. S., & Watney, W. L. (2017). Shear-wave anisotropy reveals pore fluid pressure-induced seismicity in the U.S. midcontinent. *Science Advances*, *3*(12), 1–7. https://doi.org/10.1126/sciadv.1700443

Pei, S., Peng, Z., & Chen, X. (2018). Locations of Injection-Induced Earthquakes in Oklahoma Controlled by Crustal Structures. *Journal of Geophysical Research: Solid Earth*, *123*(3), 2332–2344. https://doi.org/10.1002/2017JB014983

Qin, Y., Chen, X., Walter, J. I., Haffener, J., Trugman, D. T., Carpenter, B. M., Weingarten, M., & Kolawole, F. (2019). Deciphering the Stress State of Seismogenic Faults in Oklahoma and Southern Kansas Based on an Improved Stress Map. *Journal of Geophysical Research: Solid Earth*, *124*(12), 12920–12934. https://doi.org/10.1029/2019JB018377

Refayee, H. A., Yang, B. B., Liu, K. H., & Gao, S. S. (2014). Mantle flow and lithosphere-asthenosphere coupling beneath the southwestern edge of the North American craton: Constraints from shear-wave splitting measurements. *Earth and Planetary Science Letters*, *402*(C), 209–220. https://doi.org/10.1016/j.epsl.2013.01.031

Savage, M. K., Wessel, A., Teanby, N. A., & Hurst, A. W. (2010). Automatic measurement of shear wave splitting and applications to time varying anisotropy at Mount Ruapehu volcano, New Zealand. *Journal of Geophysical Research: Solid Earth*, *115*(12), 1–17. https://doi.org/10.1029/2010JB007722

Savage, Martha K., Ohminato, T., Aoki, Y., Tsuji, H., & Greve, S. M. (2010). Stress magnitude and its temporal variation at Mt. Asama Volcano, Japan, from seismic anisotropy and GPS. *Earth and Planetary Science Letters*, *290*(3–4), 403–414. https://doi.org/10.1016/j.epsl.2009.12.037

Segall, P., Anderson, K. R., Johanson, I., & Miklius, A. (2019). Mechanics of Inflationary Deformation During Caldera Collapse: Evidence From the 2018 Kīlauea Eruption. *Geophysical Research Letters*, *46*(21), 11782–11789. https://doi.org/10.1029/2019GL084689

Schoenball, M., & Ellsworth, W. L. (2017). Waveform-relocated earthquake catalog for Oklahoma and southern Kansas illuminates the regional fault network. *Seismological Research Letters*, *88*(5), 1252–1258. https://doi.org/10.1785/0220170083

Shah, A. K., & Keller, G. R. (2017). Geologic influence on induced seismicity: Constraints from potential field data in Oklahoma. *Geophysical Research Letters*, 152–161. https://doi.org/10.1002/2016GL071808

Shelly, D. R., & Thelen, W. A. (2019). Anatomy of a Caldera Collapse: Kīlauea 2018 Summit Seismicity Sequence in High Resolution. *Geophysical Research Letters*, *46*(24), 14395–14403. https://doi.org/10.1029/2019GL085636

Shiro, B., Burgess, M. K., Chang, J. C., Dotray, P., Okubo, P., Thelen, W. A., Waite, G. P., Antolik, L., Johanson, I. A., Anderson, K. R., & Montgomery-Brown, E. K. (2018). Earthquake sequences of the 2018 Kīlauea Volcano eruption [abs.]. *American Geophysical Union, Fall Meeting 2018 Abstracts*, abstract no. V41B-01.

Thompson, G., and Reyes, C. (2018). GISMO—A seismic data analysis toolbox for MATLAB [software package, version 1.20b]: http://doi.org/10.5281/zenodo.1404723 (accessed August 2019).

Unglert, K., Savage, M. K., Fournier, N., Ohkura, T., & Abe, Y. (2011). Shear wave splitting, vP/vS, and GPS during a time of enhanced activity at Aso caldera, Kyushu. *Journal of Geophysical Research: Solid Earth*, *116*(11), 1–14. https://doi.org/10.1029/2011JB008520

USGS. (2018). *Kīlauea Volcano – 2018 Summit and Lower East Rift Zone (LERZ) Brief Overview of Events April 17 to July 22*.

USGS. (2019). *Kilauea*. Volcano Hazards Programm. https://volcanoes.usgs.gov/volcanoes/kilauea/

Verdon, J. P., Kendall, J. M., & Wüstefeld, A. (2009). Imaging fractures and sedimentary fabrics using shear wave splitting measurements made on passive seismic data. *Geophysical Journal International*, *179*(2), 1245–1254. https://doi.org/10.1111/j.1365-246X.2009.04347.x

Waldhauser F., and Ellsworth, W. A. (2000). A double-difference earthquake location algorithm: Method and application to the northern Hayward fault. *Bulletin of the Seismological Society of America*, 90, 1353-1368.

Waldhauser, F. (2001). hypoDD: A computer program to compute double-difference hypocenter locations. *U.S. Geol. Surv. Open File Rep.*

Walsh, F. R., & Zoback, M. D. (2015). Oklahoma's recent earthquakes and saltwater disposal. *Science Advances*, *1*(5). https://doi.org/10.1126/sciadv.1500195

Walter, J. I., Ogwari, P., Thiel, A., Ferrer, F., Woelfel, I., Chang, J. C., Darold, A. P., & Holland, A. A. (2019). The Oklahoma Geological Survey Statewide Seismic Network. *Seismological Research Letters*, *March*. https://doi.org/10.1785/0220190211

Wessel, A. (2010). Automatic shear wave splitting measurements at Mt. Ruapehu volcano, New Zealand. *Master's thesis, Victoria University of Wellington, New Zealand*.

Wuestefeld, A., Kendall, J. M., Verdon, J. P., & Van As, A. (2011). In situ monitoring of rock fracturing using shear wave splitting analysis: An example from a mining setting. *Geophysical Journal International*, *187*(2), 848–860. https://doi.org/10.1111/j.1365-246X.2011.05171.x

Zaliapin, I., & Ben-Zion, Y. (2013). Earthquake clusters in southern California I: Identification and stability. *Journal of Geophysical Research: Solid Earth*, *118*(6), 2847–2864. https://doi.org/10.1002/jgrb.50179